(Hydr)oxo-bridged heme complexes: From structure to reactivity

By: Maria C. Carrasco and Shabnam Hematian

Maria C. Carrasco and Shabnam Hematian. (Hydr)oxo-bridged heme complexes: From structure to reactivity. Vol. 23, No. 11n12, pp. 1286-1307 (2019).
https://doi.org/10.1142/S1088424619300258

Abstract:

Iron–porphyrins (i.e., hemes) are present throughout the biosphere and perform a wide range of functions, particularly those that involve complex multiple-electron redox processes. Some common heme enzymes involved in these processes include cytochrome P450, heme/copper oxidase or heme/non-heme diiron nitric oxide reductase. Consequently, the (hydr)oxo-bridged heme species have been studied for the important roles that they play in many life processes or for their application for catalysis and preparation of new functional materials. This review encompasses important synthetic, structural and reactivity aspects of the (hydr)oxo-bridged heme constructs that govern their function and application. The properties and reactivity of the bridging (hydr)oxo moieties are directly dictated by the coordination environment of the heme core, the nature and ligation of the second metal center attached to the (hydr)oxo group, the presence or absence of a linker, and the degree of flexibility around that linker within the scaffold. Here, we summarize the structural features of all known (hydr)oxo-bridged heme constructs and use those to categorize and thus, provide a more comprehensive picture of structure–function relationships.

Keywords: iron porphyrins | oxo- or hydroxo-bridged heme complexes | oxo-bridged heme/non-heme | oxidative catalysis | photolysis | protonation | oxygen atom transfer | heterobinuclear | homobinuclear | ferriprotoporphyrin IX | functional materials

Article:

*****Note: Full text of article below**

Journal of Porphyrins and Phthalocyanines
J. Porphyrins Phthalocyanines 2019; **23**: 1286–1307
DOI: 10.1142/S1088424619300258

Published at https://www.worldscinet.com/jpp/

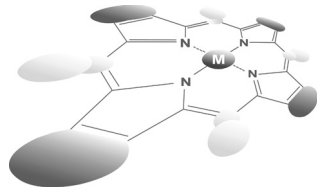

(Hydr)oxo-bridged heme complexes: From structure to reactivity

Maria C. Carrasco and Shabnam Hematian*◊

Department of Chemistry and Biochemistry, University of North Carolina at Greensboro, Greensboro 27402, USA

This paper is part of the 2019 Women in Porphyrin Science special issue.

Received 10 September 2019
Accepted date 2 November 2019

ABSTRACT: Iron–porphyrins (*i.e.,* hemes) are present throughout the biosphere and perform a wide range of functions, particularly those that involve complex multiple-electron redox processes. Some common heme enzymes involved in these processes include cytochrome P450, heme/copper oxidase or heme/non-heme diiron nitric oxide reductase. Consequently, the (hydr)oxo-bridged heme species have been studied for the important roles that they play in many life processes or for their application for catalysis and preparation of new functional materials. This review encompasses important synthetic, structural and reactivity aspects of the (hydr)oxo-bridged heme constructs that govern their function and application. The properties and reactivity of the bridging (hydr)oxo moieties are directly dictated by the coordination environment of the heme core, the nature and ligation of the second metal center attached to the (hydr)oxo group, the presence or absence of a linker, and the degree of flexibility around that linker within the scaffold. Here, we summarize the structural features of all known (hydr)oxo-bridged heme constructs and use those to categorize and thus, provide a more comprehensive picture of structure–function relationships.

KEYWORDS: iron porphyrins, oxo- or hydroxo-bridged heme complexes, oxo-bridged heme/non-heme, oxidative catalysis, photolysis, protonation, oxygen atom transfer, heterobinuclear, homobinuclear, ferriprotoporphyrin IX, functional materials.

INTRODUCTION

The characterization of a large class of oxo- and hydroxo-bridged (*i.e.,* μ-oxo and μ-hydroxo) iron porphyrin complexes has generated considerable interest in their application for catalysis and preparation of new functional materials. Additionally, iron porphyrins (*i.e.,* hemes) are present throughout the biosphere and perform a wide range of functions involving dioxygen (O_2) chemistry, such as O_2 transport or storage, O_2-mediated catalysis (*e.g.,* peroxidase, catalase, cytochromes P450 (CYPs)), and reduction of O_2 to water (*i.e.,* cytochrome *c* oxidase (C*c*O)). Consequently, the (hydr)oxo-bridged iron porphyrin species have been studied for the important roles that they play in many life processes [1, 2]. The current examples of these synthetic and biological μ-(hydr)oxo iron porphyrin constructs that are crystallographically characterized can be classified into three categories based on the nature of the second metal center attached to the μ-(hydr)oxo moiety (*i.e.,* in homo- or heterobinuclear arrangements) and its surrounding ligand environment (*i.e.,* homo- or heteroleptic frameworks), see Fig. 1.

The most common structures of μ-(hydr)oxo iron porphyrin are the μ-(hydr)oxo heme dimers in which the homobinuclear ferric sites are found in homoleptic ligand environments (Fig. 1a). The μ-oxo heme dimers, [(P)Fe^{III}–O–Fe^{III}(P)], can form from ferrous heme

◊ SPP full member in good standing

*Correspondence to: Shabnam Hematian, email: s_hemati@uncg.edu.

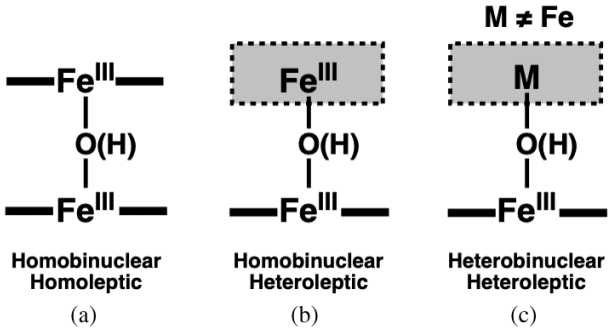

Fig. 1. Schematic bridging structures of μ-(hydr)oxo iron porphyrin constructs with homo- or heterobinuclear centers in homo- or heteroleptic frameworks

dioxygen chemistry [3] or by hydrolysis of ferric hemes in the presence of a base. No specific preference for one method over the other has been established over the years, and these methods will not be recounted here. These oxo-bridged species are known for their substantial thermodynamic stability. While in the past they were viewed as catalytically inactive species, recent reports have described them as promising oxidative catalysts capable of mimicking cytochrome P450 mono-oxygenase activity despite the lack of selectivity for a wide range of substrates including hydroxylation of C–H bonds, epoxidations, and sulfoxidation of thioether substrates. These reports are discussed in detail under the *Catalysis* and *Other Reactions* sections. Additionally, there is a growing intertest in application of μ-oxo heme dimer complexes for development of functional molecular materials such as non-linear optics (NLO), dynamic macrocyclic polymers and hydrogels, molecular cages and sensors. Many studies have also proven that the μ-oxo heme dimer complexes of ferriprotoporphyrin IX (*i.e.,* the heme cofactor of hemoglobin) contribute to important biological functions associated with some infectious diseases such as periodontitis (*i.e.,* gum disease) and malaria, *vide infra*.

The second group of μ-(hydr)oxo iron porphyrin complexes comprises those with two ferric centers, one bearing a porphyrin ring and the other with a different ligand scaffold (*i.e.,* homobinuclear complexes in heteroleptic ligand environments, Fig. 1b). There are only three examples of $[(P)Fe^{III}–O–Fe^{III}(L)]^{n+}$ constructs that are crystallographically characterized. These complexes are among synthetic models for the active site of nitric oxide reductase (NOR) which contains a μ-oxo-bridged heme/non-heme moiety in the oxidized active site. These constructs were also studied for photooxidation of various substrates.

Other examples of μ-(hydr)oxo iron porphyrin complexes encompass all the heterobinuclear complexes in which the μ-(hydr)oxo moiety bridges between a ferric heme and a non-iron metal center (*e.g.,* copper, cobalt, and chromium; see Fig. 1c). In particular, μ-(hydr)oxo heme-copper complexes have drawn more attention as biomimetic models of heme-copper oxidases such as C*c*O. Despite the significant thermodynamic stability of μ-oxo heme dimers $[(P)Fe^{III}–O–Fe^{III}(P)]$, the kinetically stable heterobinuclear $[(P)Fe^{III}–O–Cu^{II}(L)]^{n+}$ constructs can be generated through the reaction of O_2 with equimolar amounts of the corresponding reduced heme and copper complexes. They can also be synthesized by the acid–base reaction of ferric heme hydroxide compound, $[(P)Fe^{III}–OH]$, and cupric complex, $[(L)Cu^{II}]$ in the presence of a base.

The μ-oxo heme-copper complexes are able to readily oxidize nitric oxide ($NO_{(g)}$) to nitrite, which occurs through an electrophilic attack of $NO_{(g)}$ on the bridging oxo group accompanied by electron transfer (formally from $NO_{(g)}$ to the ferric heme). Detailed spectroscopic, kinetic-thermodynamic, and density functional theory (DFT) studies of this $NO_{(g)}$ oxidase activity revealed details of the reaction pathway at the molecular level, which will be briefly discussed, *vide infra*.

Oxo-bridged homobinuclear homoleptic systems: $[(P)Fe^{III}–O–Fe^{III}(P)]$

The μ-oxo heme dimers have been extensively studied over the past several decades. In 1969, Fleischer and coworkers [4], and shortly afterward Hoard and coworkers [5]–with higher resolution data–reported the first X-ray crystal structure for such oxo-bridged complexes (*i.e.,* $[(TPP)Fe^{III}–O–Fe^{III}(TPP)]$) [6–8]. Since then, over 50 additional structural datasets of various μ-(hydr)oxo heme dimers have been deposited in the Cambridge Structural Database (CSD). Table 1 summarizes some of the relevant structural parameters for these complexes that are obtained exclusively by X-ray crystallography.

In all known μ-(hydr)oxo heme dimers, each ferric center is pentacoordinated, bearing a porphyrin ring and a single bridging (hydr)oxo ligand that connects the two ferric centers. The $Fe^{III}–O–Fe^{III}$ core in these compounds is generally near-linear due to the steric requirements for two heme groups coming into close proximity [9, 10]. Notably, significant π-bonding interactions are present between the bridging oxo and the *d* orbitals of the attached ferric sites, thus their hybridization considerably deviates from sp^3 [11]. Both crystallographic and Extended X-ray Absorption Fine Structure (EXAFS) spectroscopic studies have confirmed that the Fe···Fe distances in μ-oxo heme dimers are around 3.5 Å and the ferric sites are displaced toward the oxo-bridge by about 0.5 Å from the plane defined by the four porphyrin nitrogen atoms. For example, the ferric centers in $[(TPP)Fe^{III}–O–Fe^{III}(TPP)]$ show larger out-of-plane displacement (*i.e.,* 0.50 Å) from the plane of the four coordinating nitrogen atoms compared to the corresponding five-coordinate monomer $[(TPP)Fe^{III}(H_2O)]^+$ (*i.e.,* 0.19 Å) [12]. Due to strong interactions of ferric sites with the bridging oxo moiety, the Fe–O bond lengths are also generally shorter in μ-oxo heme dimers compared with ferric

Table 1. Selected structural features and spectral data for oxo- and hydroxo-bridged heme complexes

Complex	⟨(P)Fe–O–M (°)[ε]	⟨Twist (°)[δ]	(P)Fe–O (Å)[ϡ]	(P)Fe··M (Å)[ɔ]	Fe-N_p (Å)[α,γ]	ΔN_4··Fe (Å)[Λ]	Abs. (nm)[β]	Refs.
[(TPP)Fe–O–Fe(TPP)]	174.6	35.4	1.763	3.52	2.087	0.496	408[a]	[4, 5]
[(TPP)Fe–(OH)–Fe(TPP)]($B(C_6F_5)_4$)	169.2	29.2	1.821	3.63	2.045	0.411	——	[17]
[($TPPBr_4$)Fe–O–Fe($TPPBr_4$)]	178.7	34.3	1.758	3.52	2.070	0.502	419[i]	[25, 134]
[(TTP)Fe–O–Fe(TTP)]	178.3	30.5	1.740/ 1.741	3.48	2.068/ 2.102	0.490/ 0.564	——	[135]
[(TMPyP)Fe–O–Fe(TMPyP)](ClO_4)$_8$	175.2	32.5	1.750	3.50	2.081	0.465	——	[18]
[(*p*-CTPP)Fe–O–Fe(*p*-CTPP)]	180.0	29.2	1.744	3.49	2.081	0.490	——	[136]
[(TBPP)Fe–O–Fe(TBPP)]	174.5	31.0	1.761	3.52	2.080	0.494	408[b]	[75]
[(FF)Fe–O–Fe]	161.1	24.3	1.787	3.53	2.081	0.537	409[c]	[37]
[($TPPF_5$)Fe–O–Fe($TPPF_5$)]	178.5	36.2	1.777	3.55	2.088	0.542	404[j]	[70, 137]
[(F_8TPP)Fe–O–Fe(F_8TPP)]	178.3	14.4	1.759	3.52	2.085	0.514	400[d]	[119]
[(Porphen)Fe–O–Fe(Porphen)]	156.8	22.7	1.782	3.49	2.090	0.518	——	[20]
[(OC_2OPor)Fe–O–Fe(OC_2OPor)]	180.0	28.6	1.764	3.53	2.068	0.461	410[b]	[21]
[Ru(OEP)(CO)]$_4$[Fe(*trans*-4-Py_2T_2P)]$_2$O	177.3	29.8	1.762	3.52	2.083	0.469	394[d]	[82]
[Ru(OEP)(CO)]$_4$[Fe(*cis*-4-Py_2T_2P)]$_2$O	171.4	25.8	1.747	3.48	2.057	0.483	394[d]	[82]
[(DEsP)Fe–O–Fe(DEsP)]	166.7	29.5	1.760	3.50	2.072	0.442	——	[138]
[(OEP)Fe–O–Fe(OEP)]	172.2	17.3	1.756	3.50	2.076	0.482	385[d]	[16, 139]
[(OEP)Fe–O–Fe(OEP)]	176.2	16.8	1.755	3.51	2.083	0.500	——	[16]
[(OEP)Fe–(OH)–Fe(OEP)](ClO_4)	146.2	8.4	1.938	3.71	2.039	0.381	362[d]	[16]
[(ODM)Fe–O–Fe(ODM)]	178.6	2.4	1.752	3.50	2.065	0.511	414[d]	[9]
[(din-OEP)Fe–O–Fe(din-OEP)]	172.6	18.9	1.756	3.50	2.087	0.482	378[b]	[140]
[(din-OEP)Fe–O–Fe(din-OEP)]	167.8	1.7	1.757	3.49	2.089	0.469	——	[141]
[(trn-OEP)Fe–O–Fe(trn-OEP)]	180.0	0.2	1.758	3.52	2.085	0.456	361[b]	[140]
[(tn-OEP)Fe–O–Fe(tn-OEP)]	175.1	24.2	1.772	3.54	2.095	0.545	369 [b]	[140]
[(tn-OEP)Fe–O–Fe(tn-OEP)]	176.9	21	1.772	3.54	2.088	0.528	369 [b]	[140]
[(TCPP)Fe–O–Fe(TCPP)]	179.8	33.6	1.760	3.52	2.083	0.462	361[h]	[71]
[(PPIXDME)Fe–O–Fe(PPIXDME)]	170.4	27.2	1.748	3.48	2.078	0.416	——	[10]
[(DEP)Fe–O–Fe]	152.0	1.0	1.780	3.45	2.083	0.522	344[d]	[46]
[(ETA)Fe–O–Fe]·CH_3CN	147.9	16.1	1.774	3.41	2.068	0.519	——	[43]
[(ETA)Fe–O–Fe]·C_7H_8	151.2	16.3	1.768	3.42	2.077	0.500	——	[43]
[(ETA)Fe–(OH)–Fe](SbF_6)	152.1	16.4	1.937	3.76	1.976	0.292	376[d]	[142]
[(ETA)Fe–(OH)–Fe](I_3)	142.5	12.9	1.934/ 1.897	3.63	2.007/ 2.051	0.405/ 0.451	380[d]	[143]
[(ETA)Fe–(OH)–Fe](BF_4)	148.6	14.8	1.925/ 1.967	3.75	2.020/ 1.967	0.363/ 0.307	380[d]	[144]
[(ETA)Fe–(OH)–Fe](ClO_4)	141.2	10.8	1.911/ 1.922	3.62	2.063/ 2.054	0.469/ 0.422	372[d]	[144]
[(ETE)Fe–O–Fe]	150.9	0.6	1.783	3.45	2.080	0.532	394[d]	[45]
[(ETE)Fe–(OH)–Fe](ClO_4)	143.8	5.6	1.943	3.69	2.048	0.401	371[d]	[145]
[(ETE)Fe–(OH)–Fe](I_5)	142.4	2.5	1.924/ 1.920	3.64	2.056/ 2.048	0.456/ 0.437	377[d]	[145]
[(ETE)Fe–(OH)–Fe](TNP)	147.3	3.2	1.914	3.67	2.062	0.460	363[d]	[48]
[(DPD)Fe–O–Fe]	158.8	1.5	1.782	3.5	2.105	0.565	395[a]	[38,40]
[(DPXM)Fe–O–Fe]	155.2	3.7	1.789	3.49	2.087	0.566	——	[41]
[(DPA)Fe–O–Fe]	165.7	0.7	1.759	3.49	2.085	0.483	——	*

(*Continued*)

Table 1. (*Continued*)

Complex	⟨(P)Fe–O–M (°)[ε]	⟨Twist (°)[δ]	(P)Fe–O (Å)[ϡ]	(P)Fe··M (Å)[ϖ]	Fe-N_p (Å)[α,γ]	ΔN_4··Fe (Å)[Λ]	Abs. (nm)[β]	Refs.
[(DPX)Fe–O–Fe]	175.8	3.0	1.763	3.52	2.074	0.512/ 0.452	——	*
[(^{6}L)Fe–O–Fe(X)](PF_6)[å]	166.6	——	1.785	3.56	2.074	0.537	416[d]	[104]
[(^{5}L)Fe–O–Fe(Cl)](ClO_4)	157.5	——	1.767	3.48	2.084	0.503	413[d]	[103, 146]
[(F_8TPP)Fe–O–Fe(Cl)(TMPA)](ClO_4)	156.6	——	1.777	3.47	2.095	0.464	411[d]	[103, 104]
[(NCH_3TPP)Fe-O-Fe(TPP)](ClO_4)	165.3	30.2	1.741/ 1.767	3.48	2.107/ 2.067	0.546/ 0.441	414[l]	[97, 147]
[(TMP)Fe–O–Cu(5MeTPA)] ($B(C_6F_5)_4$)	172.8	——	1.760	3.61	2.115	0.601	442[k]	[115]
[(TMPP)Fe–O–Cu(TMPA)]($B(C_6F_5)_4$)	173.5	——	1.720	3.54	2.102	0.548	443[e]	[129]
[(F_8TPP)Fe–O–Cu(TMPA)](ClO_4)	178.2	——	1.740	3.60	2.105	0.554	435[e]	[108, 125]
[(F_8TPP)Fe–O–Cu($MePY_2$)]($B(C_6F_5)_4$)	142.5	——	1.756	3.41	2.094	0.553	438[e]	[125]
[(F_8TPP)Fe–O–Cu(L^{Me_2N})]($B(C_6F_5)_4$)	143.5	——	1.747	3.42	2.096	0.550	449[f]	[120]
[(F_8TPP)Fe–O–Cu(AN)](CF_3O_3S)	149.5	——	1.746	3.44	2.090	0.507	440[g]	[124]
[(^{6}L)Fe–O–Cu]($B(C_6F_5)_4$)	171.1	——	1.749	3.59	2.103	0.579	424[c]	[110]
[(OEP)Fe–O–Cu(Me_6tren)](ClO_4)	176.6	——	1.744	3.57	2.112	0.581	427[d]	[109]
[(OEP)Fe–(OH)–Cu(Me_5dien) ($OClO_3$)](ClO_4)	157.1	——	1.928	3.81	2.042	0.414	——	[118]
[(TPP)Fe–O–Cr(Pip)(TPP)]	177.7	29.7	1.751	3.53	2.097	0.533	427[a]	[131]
[(TMPP)Fe–O–Cr(Py)(TPP)]	178.0	32.0	——	3.60	——	——	424[a]	[130]
[(F_8TPP)Fe–O–Co(TMPA)](ClO_4)	171.6	——	1.747	3.58	2.110	0.562	437[d]	[132]
{Au_8(μ-PAnP)$_4$[(TPyP)Fe–O–Fe (TPyP)]}(CF_3O_3S)$_8$	157.8	19.9	1.752	3.44	2.030	0.428	412	[80]
[(TPP)Fe–O–Fe(TPP)]·C_{60}	173.7	30.3	1.758	3.51	2.078	0.467	——	[77]
[(TPP)Fe–O–Fe(TPP)]·C_{70}	180.0	29.0	1.756	3.51	2.083	0.490	——	[78]
[(OEP)Fe–O–Fe(OEP)]·C_{60}	150.2	28.7	1.773	3.43	2.098	0.515	——	[76]

[Λ]Iron displacement from the porphyrin's nitrogen plane (N_4); [α]Nitrogen atoms forming porphyrin core (N_p); [β]UV-vis absorption (Soret band); [γ]Average of eight (or four) Fe–N bond distances; [δ]Degree of torsion (twist) between two porphyrin rings; [ε]Degree of bending in the heme iron–oxo–metal ((P)Fe–O–M) moiety; [ϡ]Bond distance between the heme-iron and bridging O-atom; average of two bonds unless two distances are stated; [ϖ]Heme iron to metal bond distance; *CSD Private Communication; [å]Ligand X^- represents chloride or methoxide; [a]Benzene; [b]Chloroform; [c]Toluene; [d]Dichloromethane; Acetone; [f]6% Propionitrile : 94% Dichloromethane; [g]Tetrahydrofuran; [h]*n*-Dimethylformamide; [i]Benzonitrile; [j]Methanol; [k]Acetonitrile; [l]Dichloroethane; [m]10% Methanol : 90% Chloroform.

axial ligand distances in corresponding monomer complexes. The μ-oxo heme dimers are also electron paramagnetic resonance (EPR)-silent because of strong antiferromagnetic coupling between the two high-spin ($S = {}^5/_2$) ferric sites [13]. ^{57}Fe Mössbauer spectroscopy, Evans nuclear magnetic resonance (NMR) method, and superconducting quantum interference device (SQUID) magnetometry measurements have confirmed the large antiferromagnetic coupling constants (J = -120 to -140 cm^{-1}) for these bridging complexes that is directly correlated with their nearly linear Fe–O–Fe cores and relatively short Fe–O distances (~1.75 Å) [14, 15].

The bridging oxo moieties in μ-oxo heme dimers are commonly basic and, upon protonation, which is generally accompanied by varying degrees of re-hybridization, form the corresponding bent μ-hydroxo heme dimers [16]. For comparison, the Fe–O–Fe angle of 172° in [(OEP)Fe^{III}–O–Fe^{III}(OEP)] is significantly decreased upon protonation (*i.e.,* Fe–(OH)–Fe angle of the corresponding μ-hydroxo heme dimer is 146°) [16], while in some cases such as [(TPP)Fe^{III}–O–Fe^{III}(TPP)] protonation of the bridging oxo only slightly changes the Fe–O(H)–Fe core angle (*i.e.,* <5°; see Fig. 2 and Table 1) [17]. It is noteworthy that the two porphyrin cores in [(TPP)Fe^{III}–(OH)–Fe^{III}(TPP)]$^+$ adopt ruffled-type conformations in which opposite pyrrole rings are counter-rotated in a way that the *meso* carbons are alternatively displaced upward and downward with respect to the mean of the porphyrin planes (Fig. 2).

Another important structural parameter in μ-(hydr)oxo heme dimers is the N_p–Fe–Fe′–N'_p dihedral angle (*i.e.,* twist angle). The two possible extreme conformations are eclipsed (*i.e., D_{4h}* symmetry and twist angle = 0°) and staggered (*i.e., D_{4d}* symmetry and twist angle = 45°). The smaller average twist angle for [(OEP)Fe^{III}–O–Fe^{III}(OEP)] (~17°) compared with that of [(TPP)Fe^{III}–O–Fe^{III}(TPP)] (~35°), and other *meso*-substituted μ-oxo heme dimers can be interpreted in terms of steric hindrance between

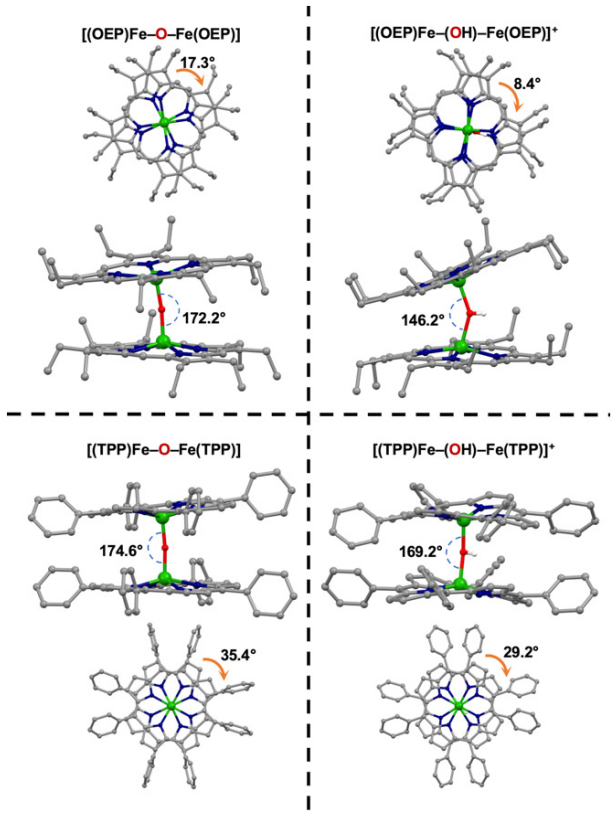

Fig. 2. Side-by-side views of μ-oxo and μ-hydroxo heme dimers, $[(P)Fe^{III}–O(H)–Fe^{III}(P)]^{n+}$ (n = 0 or 1), with the OEP or TPP frameworks, displaying their structural differences such as the Fe–O–Fe moiety angles and twist angles

the bulky peripheral substituents which is absent in the μ-oxo heme dimer bearing the OEP frameworks. The facing porphyrin rings in all derivatives of $[(TPP)Fe^{III}–O–Fe^{III}(TPP)]$ are also considerably rotated with respect to each other so that peripheral phenyl rings are almost staggered, see Fig. 2. Thus, the twist angle is a sensitive function of the peripheral substituents and interplanar spacing.

In addition to the extensive number of studies on organic-soluble μ-oxo heme dimers, many synthetic water-soluble derivatives have also been prepared [18, 19]. For these derivatives the bulky peripheral groups can also deter the aggregation process while water solubility can be achieved through charged peripheral substituents such as the negatively charged sulfonates in $[(TPPS)Fe^{III}–O–Fe^{III}(TPPS)]^{8-}$ or the positively charged methylpyridinium groups in $[(TMPyP)Fe^{III}–O–Fe^{III}(TMPyP)]^{8+}$. The structural features of the water-soluble μ-oxo heme dimers are mostly comparable with their organic-soluble counterparts, see Table 1.

A large variety of additional modifications on the heme cores have led to a number of other novel μ-oxo heme dimer structures. For example, efforts for introduction of a potential second metal binding site in a phenanthroline-strapped porphyrin framework or attempts for providing a barrier above the porphyrin ring in "capped" porphyrins resulted in the discovery of the very bent μ-oxo moiety in $[(Porphen)Fe^{III}–O–Fe^{III}(Porphen)]$ [20] and perfectly linear arrangement in $[(OC_2OPor)Fe^{III}–O–Fe^{III}(OC_2OPor)]$ [21], see Table 1.

The electronic absorption spectra of μ-oxo heme dimers are blue-shifted relative to their corresponding ferric heme monomers. For example, in dichloromethane (DCM), the Soret band of dimeric $[(OEP)Fe^{III}–O–Fe^{III}(OEP)]$ is at 385 nm while that of monomeric $[(OEP)Fe^{III}(ClO_4)]$ is at 389 nm. Additionally, the UV-vis spectrum of the protonated dimer, $[(OEP)Fe^{III}–(OH)–Fe^{III}(OEP)]$ shows a strongly blue-shifted Soret band at 362 nm [16], see Table 1. These blue shifts of the electronic absorption spectra are ascribed to the excitation coupling between the two heme chromophores which are diagnostic of dimeric constructs with the cofacial orientations.

Electrochemistry. A number of studies have suggested that the stepwise first and second one-electron reduction of the μ-oxo diferric heme dimers are metal-centered. The first electrochemical reduction yields a paramagnetic ferric-ferrous μ-oxo heme dimer intermediate (g = 1.95) followed by the second reduction step to generate a fully reduced high-spin ferrous–ferrous μ-oxo heme dimer intermediate [22–26]. These dimer species have been postulated based on a combination of electrochemical analysis and the data obtained from surface-enhanced Raman scattering (SERS), UV-vis absorption and EPR spectroscopies. However, there appear to be some disagreements in the literature over the exact nature of the bridging group (*i.e.,* μ-oxo or -hydroxo) in these dimeric intermediates [27].

Furthermore, cyclic voltammetry of μ-oxo heme dimers such as $[(TPP)Fe^{III}–O–Fe^{III}(TPP)]$ show two chemically reversible one-electron oxidation processes and in most cases both oxidations appear to take place on porphyrin cores rather than iron centers [15]. The products of these oxidations have not been structurally characterized, but spectroscopic and magnetic measurements strongly support formation of the porphyrin π-cation radical with strong antiferromagnetic coupling to the ferric center [28–30].

Tethered systems. Cofacial or "Pacman" type porphyrin systems have a rich history in catalyzing multielectron redox reactions of small molecules (*e.g.,* four electron reduction of O_2 to water) [31, 32]. Consequently, the chemistry of tethered μ-(hydr)oxo heme dimers where the two porphyrin rings are covalently connected have drawn considerable interest in recent years and have been meticulously reviewed elsewhere [33–36]. Both "rigid" and "flexible" linkers of variable lengths have been used for controlling the Fe···Fe distance and degree of opening and closing within the cofacial cleft, see Chart 1.

Reed and coworkers reported the first example of a *bis*-iron(III)-μ-oxo cofacial porphyrin [37]. The urea-linked *bis*-tetraphenyl porphyrin (FF) accommodates a bent Fe–O–Fe angle of 161° possibly due to the

hydrogen-bonding network of two water molecules between the bridging oxo moiety and hydrogen atoms of the urea linker, see Chart 1. The FF scaffold also allows significant rotational flexibility for the tethered porphyrin rings as evidenced by the twist angle of 24°. Later, Nocera and coworkers prepared a host of *bis*-iron(III)-μ-oxo cofacial porphyrins bearing rigid linkers such as dibenzofuran (*i.e.*, DPD, DPDM and DPDF) and xanthene (*i.e.,* DPX and DPXM) [38–42]. Unlike other μ-oxo heme dimers, rotation of the two heme cores with respect to each other is restricted by the rigid dibenzofuran or xanthene linker (Chart 1), thereby creating an almost eclipsed conformation with a twist angle of less than 4° (Table 1). Interestingly, these tethered platforms with rigid linkers can house a variety of Fe–O–Fe angles, from a near-linear μ-oxo structure in DPX (*i.e.,* 176°) to a bent Fe–O–Fe angle of 155° in DPXM.

To bring the two ferric sites in closer contact, Rath and coworkers prepared alternative cofacial constructs bearing linkers with different degrees of flexibility (*i.e.*, ethane-, ethene-, and pyrrole-bridged μ-oxo heme dimers, see Chart 1) [43–46]. Perhaps the most striking features of these *bis*-iron(III)-μ-oxo constructs are their small cleft size which directly translates to the very bent Fe–O–Fe angle of about 150° and shorter Fe···Fe distance (*i.e.,* ≤ 3.45 Å) compared to other known μ-oxo heme dimers, see Table 1. The highly flexible ethane linker in the ETA framework allows for the heme cores to make a 16° twist angle to minimize the steric hindrance of the ethyl groups. In turn, the relatively less flexible pyrrole linker in the DEP framework or the rigid ethene linker in the ETE scaffold restricts the free rotation of the attached heme cores, thus holding them in a fully eclipsed conformation (*i.e.,* twist angle of ≤1°). A series of *bis*-iron(III)-μ-hydroxo cofacial porphyrins of this group (*i.e.,* ETA, ETE, and DEP) have been generated from protonation of the corresponding μ-oxo complexes by addition of strong Brønsted acids with non- or weakly coordinating conjugate bases (*e.g.,* BF_4^-, PF_6^-, SbF_6^-, ClO_4^-, and I^-). In these tethered systems, further bending of the Fe–O(H)–Fe angle upon protonation is also observed; consequently, the two heme cores further approach each other. The extreme closeness of the two heme chromophores leads to even more substantial blue-shifting in the *bis*-iron(III) μ-hydroxo cofacial porphyrins compared to their μ-oxo counterparts. Another interesting observation is the lack of equivalency of the spin states in the attached heme cores of these tethered μ-hydroxo systems. The computational and spectroscopic studies point to varying degrees of interaction between the linked ferric hemes and different counter anions that may result in subtle environmental perturbations in one of the ferric sites. These asymmetric interactions are generally governed by the size, charge, and nature of the anions, which consequently can lead to increased ring deformation and modulation of the spin state of one of the two ferric heme cores. For instance, the

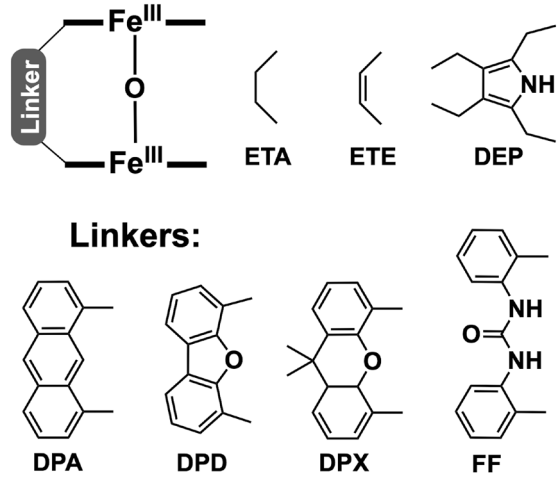

Chart 1. Schematic representation of tethered μ-oxo heme dimers bearing "rigid" or "flexible" linkers

bis-iron(III)-μ-hydroxo cofacial porphyrins with I_3^- or I_5^- counterions, possess one high-spin ferric site ($S = {}^5/_2$) along with a second ferric site with admixed-intermediate spin state ($S = {}^3/_2$ with a minor contribution from $S = {}^5/_2$).

The stochiometric reaction of a weaker acid such as 2,4,6-trinitrophenol (HTNP) with [(ETE)Fe^{III}–O–Fe^{III}] generates the μ-hydroxo adduct, [(ETE)Fe^{III}–(OH)–Fe^{III}]·(TNP) in which the planar structure of the phenoxide group fits within the cofacial cleft cavity, therefore forming a fairly strong hydrogen bond with the bridging hydroxo moiety (*i.e.,* $O_1 \cdots O_8$ distance is 2.58 Å and C–O_8 bond length is 1.24 Å) [47], see Fig. 3. Interestingly,

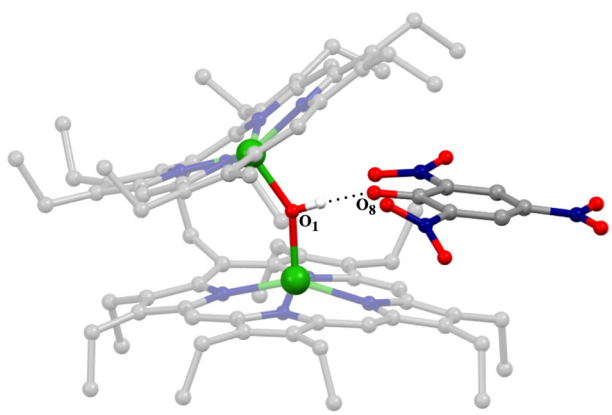

Fig. 3. X-ray crystal structure of the *bis*-iron(III)-μ-hydroxo cofacial porphyrin, [(ETE)Fe^{III}–(OH)–Fe^{III}], and 2,4,6-trinitrophenoxide adduct with a fairly strong hydrogen bond between the phenoxide group and the bridging hydroxo moiety. Recreated with permission from [48]. Copyright 2016 John Wiley & Sons, Inc.

the two ferric centers in this adduct are equivalent in the solid state (high-spin state; $S = {}^5/_2$) and both convert to intermediate spin ($S = {}^3/_2$) in solution as observed by ^{1}H NMR spectroscopy. The results from

several DFT calculations were also in agreement with the experimentally observed ferric spin crossover triggered by hydrogen bonding. Further titration of the [(ETE)Fe^{III}–(OH)–Fe^{III}]·(TNP) with the second equivalent of the phenol results in breakage of the bridging hydroxo moiety and formation of one water molecule. This is accompanied by coordination of one of the resulting phenoxide groups to each ferric site forming [(ETE)Fe^{III}_2(TNP)$_2$] [48]. Hendrickson and Wollmann also reported a similar observation for the reaction of excess organic acids with the untethered μ-oxo complex, [(TPP)Fe^{III}–O–Fe^{III}(TPP)] [49, 50].

Catalysis. Several tethered and untethered μ-oxo heme systems have been studied for both photochemical and thermochemical catalytic oxidations of a variety of substrates under different conditions. In all cases, the ferryl heme species are widely invoked as key oxidizing intermediates that are formed during the catalytic cycles proceeded by heterolytic cleavage of the Fe–O–Fe moiety [15]. Furthermore, a common unwanted side reaction is self-degradation of the heme sites due to attack of these highly reactive intermediates on the porphyrin ring itself.

The first examples of the photolysis of μ-oxo heme dimers were provided by Richman and Peterson in the 1980s. The authors showed that direct excitation of the O → Fe ligand-to-metal charge transfer (LMCT) band (λ_{max} = 320 nm) leads to photochemical disproportionation of [(TPP)Fe^{III}–O–Fe^{III}(TPP)] into the corresponding ferrous and oxo-ferryl monomers (*i.e.,* [(TPP)Fe^{II}] and [(TPP)Fe^{IV}=O]) [51–53]. The resulting ferryl heme monomer represents a strong oxidant that is capable of substrate oxidation through an oxygen atom transfer reaction [54]. Subsequently, the second equivalent of ferrous heme is formed, and the μ-oxo heme dimer is regenerated in the presence of O_2, thus the process becomes catalytic. By photolyzing [(TPP)Fe^{III}–O–Fe^{III}(TPP)] in the presence of O_2, catalytic oxidation of a wide range of substrates such as alkyl and aryl phosphines, amines and olefins was accomplished [55, 56].

Furthermore, the picosecond absorption studies of the photoexcitation of [(TPP)Fe^{III}–O–Fe^{III}(TPP)] by Rentzepis and coworkers revealed the presence of a very short-lived intermediate with a lifetime of <100 ps which was described as an excited state localized to a monomer unit. Subsequently, this intermediate converts mainly to the photodissociated pair [(TPP)Fe^{III}]$^+$ plus [(TPP)Fe^{III}–O]$^-$ and, to a lesser extent, forms the photodisproportionation products, [(TPP)Fe^{II}] and [(TPP)Fe^{IV}=O], see Scheme 1. In the absence of substrates, the recombination of the photoproducts takes place in less than 5 ns, regenerating the starting μ-oxo heme dimers [57]. Later, resonance Raman (RR) studies further confirmed the formation of the five-coordinate low-spin oxo-ferryl (*i.e.,* [(TPP)Fe^{IV}=O]) from the photodisproportionation of [(TPP)Fe^{III}–O–Fe^{III}(TPP)] in a detergent micelle at room temperature (*e.g.,* Fe^{IV}=O vibrational frequency (ν_{FeO}) is at 843 cm^{-1}) [58].

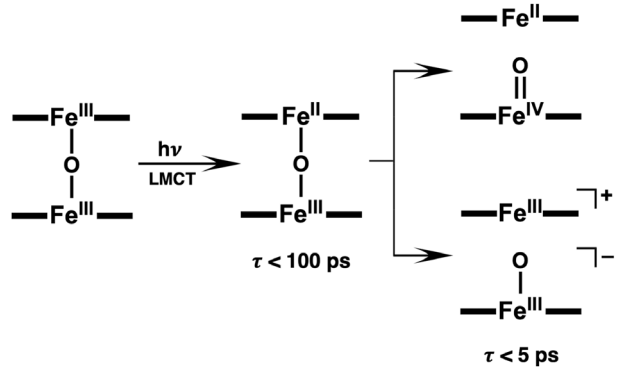

Scheme 1. Two chemically feasible photoproducts (*i.e.*, the photodisproportionation products (top) and photodissociated pair (bottom)) resulting from LMCT excitation of μ-oxo heme dimers

Nocera and coworkers have done considerable research on the photophysics of a number *bis*-iron(III)-μ-oxo "Pacman" porphyrin systems [32]. In order to understand the effect of a spring-loaded cleft on the photoinduced oxygenation of substrates, a comparative reactivity study of two tethered (*i.e.,* DPD and DPX) and one untethered (*i.e.,* etioporphyrin abbreviated as Etio) *bis*-iron(III)-μ-oxo porphyrin systems was performed [39]. The results of the stoichiometric oxygenation reactions of dimethyl sulfide (DMS) revealed that the product quantum yields for formation of both dimethyl sulfoxide (DMSO) and dimethyl sulfone ($DMSO_2$) increase in the order of: [(DPX)Fe^{III}–O–Fe^{III}] < [(Etio)Fe^{III}–O–Fe^{III}(Etio)] < [(DPD)Fe^{III}–O–Fe^{III}]. According to this observation, the authors proposed that the significant vertical flexibility of the DPD platform triggers the "molecular spring" action of [(DPD)Fe^{III}–O–Fe^{III}], which can hinder recombination and regeneration of the starting *bis*-iron(III)-μ-oxo porphyrin system to some extent and/or support a side-on approach of substrate to the oxo-ferryl intermediate. Subsequently, the transient absorption study showed that the cage escape yield is generally low, even for the untethered system [40]. The results suggested that the quantum yields of photocatalytic oxidation of substrates may be significantly increased if the escape yield of photodisproportionation intermediates (*i.e.,* Fe^{II}/Fe^{IV}=O pair) can be improved.

Later, a modified DPD platform bearing three pentafluorophenyl groups in the *meso* positions of the porphyrin rings (DPDF) was investigated [42]. The electron-withdrawing peripheral substituents enhance the oxidizing power of the photogenerated oxo-ferryl species, therefore the corresponding *bis*-iron(III)-μ-oxo porphyrin system catalyzes the aerobic photochemical oxidation of phosphines, sulfides, olefins, and hydrocarbons with higher turnover numbers [42, 59]. Notably, the presence of the ancillary pentafluorophenyl groups in the [(DPDF)Fe^{III}–O–Fe^{III}] system also lowers the susceptibility of the porphyrin to oxidative decomposition and induces the

photoreaction at longer wavelengths in the visible region ($\lambda_{exc} > 425$ nm) [42, 59]. The photochemical efficiency of substrate oxidation also diminishes with an increase in the steric bulk of the substrates, due to limited access to cleft of the "Pacman" scaffold and active oxidant.

Turning next to the ethane- and ethene-bridged μ-oxo heme dimers, Rath and coworkers reported both stoichiometric and catalytic photochemical oxidation of organophosphites (*i.e.,* $P(OR)_3$; R = Me, Et) under anaerobic and aerobic conditions, respectively. The [(ETE)Fe^{III}–O–Fe^{III}] platform with the rigid ethene linker shows higher photochemical catalytic efficiency [43–45].

The first reports of related studies on thermochemical catalytic oxidation of hydrocarbons (*e.g.,* hydroxylation of cyclohexane or 2-methylbutane) using [(TPP)Fe^{III}–O–Fe^{III}(TPP)] with iodosobenzene (PhIO) as a terminal oxidant were published by Guo in 1994. The author also evaluated the effect of peripheral substituents (electron-donating *vs*. electron-withdrawing), reaction temperature, solvent, and exposure to air on the catalytic activity of the μ-oxo heme dimers [60–62]. Later, the application of μ-oxo heme dimers for direct aerobic oxidation of other hydrocarbons (*e.g.,* cyclopentane, cyclooctane, ethylbenzene or toluene), with the O_2 serving as the terminal oxidant, was investigated [63–65]. Guo and coworkers subsequently examined the influence of dioxygen pressure and flow rate in the homogeneous liquid-phase aerobic oxidation of toluene to benzaldehyde, benzyl alcohol, and benzoic acid under conditions similar to those of commercial operations. Their results from semi-batch and continuous operation mode reveal that at O_2 partial pressure lower than 0.070 MPa at 190 °C, the oxidation of toluene is directly limited by the concentration of dissolved O_2, whereas the oxidation rate of toluene is zero-order with respect to O_2 at higher partial pressures. Moreover, they showed that the sequential decrease of temperature in a series of three stirred-tank reactors could significantly increase the selectivity and yield of benzaldehyde and benzyl alcohol up to about 17 and 44%, respectively [66, 67].

Despite extensive reports on the thermochemical oxidation of substrates using μ-oxo heme dimers, the intricate nature and mechanism of formation of the putative ferryl intermediate(s) involved are still unclear. The μ-oxo heme dimers are generally regarded as thermally inert species that show little or no tendency toward thermochemical disproportionation. However, a recent study by Meyer and coworkers shows that a non-heme *bis*-iron(III)-μ-oxo with macrocyclic tetracarbene (L^{NHC}) ligation, [(L^{NHC})Fe^{III}–O–Fe^{III}(L^{NHC})]$^{4+}$, thermally disproportionates in an acetonitrile solution into the oxo-ferryl and ferrous components. The disproportionation equilibrium for this μ-oxo complex in the dark, although very small (*i.e.,* $K_{eq} = 7.5 \times 10^{-8}$ M), is non-zero and translates to a Gibbs free energy change (ΔG°) of about 40 kJ·mol^{-1} (*i.e.,* 9.6 kcal·mol^{-1}) at room temperature [68]. A similar disproportionation equilibrium may be responsible for the observed thermochemical reactivity of μ-oxo heme dimers toward a wide range of substrates.

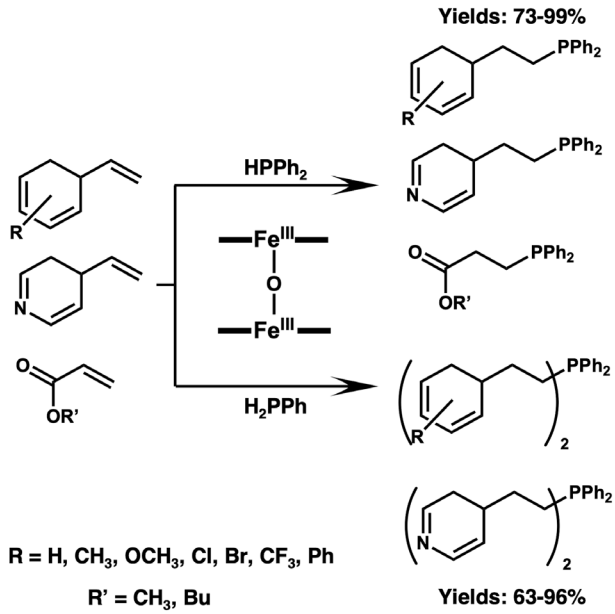

Fig. 4. Hydrophosphination of some activated alkenes with activated primary (H_2PPh) or secondary ($HPPh_2$) phosphines catalyzed by [(TPP)Fe^{III}–O–Fe^{III}(TPP)] as reported in [69]

Other reactions. The μ-oxo heme dimers have also been explored for other redox and acid-base reactions. For example, Webster and coworkers reported that μ-oxo heme dimers, such as [(TPP)Fe^{III}–O–Fe^{III}(TPP)], can readily catalyze the hydrophosphination of styrene derivatives and effect one or two consecutive activation reactions on the primary phosphines to form secondary or tertiary products in modest to excellent yields [69], see Fig. 4. The electron-deficient analogue of the TPP platform with the pentafluorophenyl *meso*-substituents in [($TPPF_5$)Fe^{III}–O–Fe^{III}($TPPF_5$)] has been utilized for an oxidative desulfurization process of a model oil containing the representative refractory sulfur compounds in petroleum such as dibenzothiophene and its derivatives. The catalytic system operates in a biphasic medium at room temperature and in the presence of H_2O_2 as the terminal oxidant forming the corresponding sulfoxides and sulfones [70].

Another example of the μ-oxo heme dimers developed for catalyzing redox processes is [(TCPP)Fe^{III}–O–Fe^{III}(TCPP)]. Here, the peripheral carboxylic groups form a network of hydrogen bonds between porphyrin planes of neighboring μ-oxo heme dimers creating a two-dimensional (2D) array. Subsequently, the 2D arrays are stacked along the (001) direction supporting the interlayer π–π interactions (interlayer distance is about 3.7 Å) and ultimately form a continuous three-dimensional (3D) porous network, see Fig. 5.

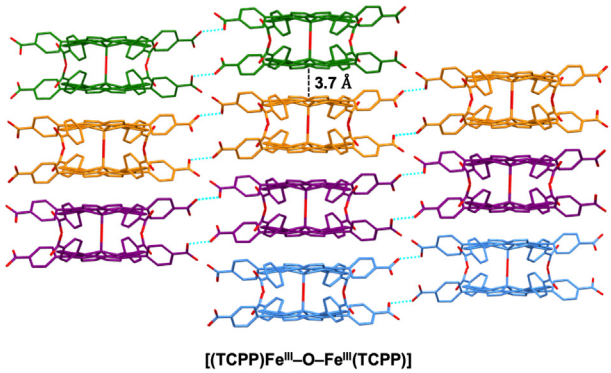

Fig. 5. Stacking of hydrogen bonded 2D layers of the [(TCPP)Fe^{III}–O–Fe^{III}(TCPP)] units through π–π interactions (about 3.5 to 3.9 Å) among the dimers of each layer. Adapted with permission from [71]. Copyright 2015 Royal Society of Chemistry

The resulting coordination network exhibits moderate heterogeneous catalytic activity for the oxidation of alcohols to aldehydes. Remarkably, the μ-oxo heme dimer scaffold plays a dual role as both the catalyst and supramolecular synthon in the catalytic network [71].

Reactivity of a series of μ-oxo heme dimers toward various nitrogen oxides (*e.g.,* nitric oxide ($NO_{(g)}$), dinitrogen tetroxide (N_2O_4), and dinitrogen trioxide (N_2O_3)) have also been studied by Fanning, Scheidt and coworkers [72, 73]. The reaction of the [(TPP)Fe^{III}–O–Fe^{III}(TPP)] complex with $NO_{(g)}$ in toluene yields the nitro-nitrosyl complex, [(TPP)Fe^{III}(NO_2)(NO)], while its reaction with N_2O_4 or N_2O_3 in toluene produces the corresponding ferric heme nitrate (*i.e.,* [(TPP)Fe^{III}(NO_3)]) [72]. Moreover, the μ-oxo heme dimers can serve as precursors for the preparation of a host of bridged heme dimer species through the acid–base reactions. An example for such species is the first structurally characterized heme hyponitrite adduct, [(OEP)Fe^{III}–($N_2O_2^{2-}$)–Fe^{III}(OEP)], which was generated by the reaction of the corresponding μ-oxo heme dimers (*i.e.,* [(OEP)Fe^{III}–O–Fe^{III}(OEP)]) with hyponitrous acid ($H_2N_2O_2$) accompanied by the release of a water molecule [74].

Applications in functional molecular materials. The μ-oxo heme dimer is a versatile platform for additional substitutions and the construction of preorganized frameworks; therefore there is a growing intertest in the potential application of μ-oxo heme dimer complexes in the field of functional molecular materials. It has been shown that the nonlinear optical properties of the μ-oxo heme dimers are superior in comparison with the corresponding monomers due to their more delocalized π-conjugated systems. For example the self-assembled nanostructures of the [(TBPP)Fe^{III}–O–Fe^{III}(TBPP)] complex are endowed with remarkable third-order nonlinear optical (NLO)

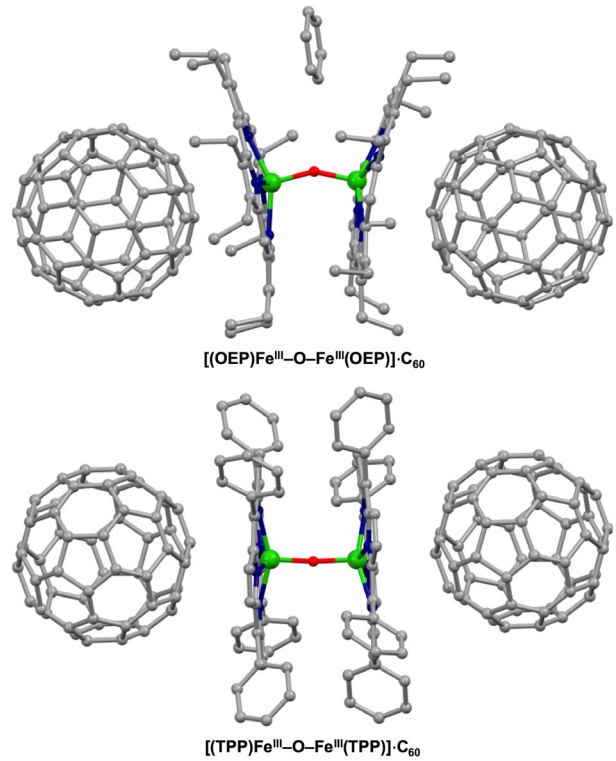

Fig. 6. Molecular structures of [(P)Fe^{III}–O–Fe^{III}(P)]·C_{60} complexes in which a μ-oxo heme dimer is packed between two fullerene molecules. Recreated with permission from [76, 77]. Copyright 2003 American Chemical Society and 2016 John Wiley & Sons, Inc.

properties and show almost an order of magnitude larger two-photon absorption (TPA) cross-section value than that of the monomer [75].

Additionally, efforts for development of photo-active materials for photovoltaic and light-harvesting applications have led to interesting μ-oxo-heme-dimer-fullerene supramolecular architectures. These fullerene-adducts generally exhibit intense charge transfer (CT) bands in the visible range due to effective overlap of their highest occupied molecular orbital (HOMO) and lowest unoccupied molecular orbital (LUMO) between the concave surfaces of the five-coordinate porphyrin moieties and spherical fullerene molecules. Balch and coworkers cocrystallized the [(OEP)Fe^{III}–O–Fe^{III}(OEP)] complex with fullerene in benzene. The Fe–O–Fe angle in [(OEP)Fe^{III}–O–Fe^{III}(OEP)]·C_{60}·C_6H_6 is markedly bent at 150° and a benzene molecule inserted into the space between the two porphyrin rings, see Fig. 6. Thus, the significant variation for the Fe–O–Fe angle in the supramolecular assembly and starting μ-oxo heme dimer (⟨Fe–O–Fe = 172°) reveals that the bridging oxo moiety in these platforms is rather flexible and can be varied by a combination of intermolecular interactions and crystal packing forces [76]. Cocrystallization of [(TPP)Fe^{III}–O–Fe^{III}(TPP)] with the spherical C_{60} fullerene also

forms a neutral solid-state supramolecular architecture with significantly modified optical properties. The Fe–O–Fe angle in the $[(TPP)Fe^{III}–O–Fe^{III}(TPP)]\cdot C_{60}$ is similar to that of the parent compound, see Fig. 6 and Table 1 [77]. Moreover, the complexation of the $[(TPP)Fe^{III}–O–Fe^{III}(TPP)]$ with the ellipsoidal C_{70} fullerene has been studied by Lyubovskaya and coworkers. A close examination of molecular packing of $[(TPP)Fe^{III}–O–Fe^{III}(TPP)]\cdot C_{70}$ reveals that at room temperature, freely rotating C_{70} molecules occupy the large cavities formed by the μ-oxo heme dimers, whereas at lower temperature ($T \leq 100$ K) the appearance of additional Van der Waals forces significantly reduces the size of those vacancies, thus hindering the rotation of C_{70} molecules [78].

The water-soluble μ-oxo heme dimer $[(TMPyP)Fe^{III}–O–Fe^{III}(TMPyP)]^{8+}$ has also been used to induce aggregation of the solid or hollow gold nanospheres into a plasmonic nanoparticle network. Detailed spectroscopic and microscopic measurements of the resulting plasmonic nanoparticle networks supported the "edge-on" configuration in which both heme planes of the μ-oxo heme dimer align parallel to the interparticle axis, thus separating the gold nanoparticles by about 1.5 nm, which consequently leads to a red-shifted coupled plasmon mode [79]. Here, four methylpyridinium groups (two from each porphyrin ring) are electrostatically adsorbed on the surface of each nanoparticle, see Fig. 7.

Yip and coworkers have recently reported a pH-responsive molecular cage that can reversibly undergo conformational transitions shown in Fig. 8. The molecular cage, $\{Au_8(\mu\text{-}PAnP)_4[(TPyP)Fe^{III}(H_2O)_2]_2(CF_3O_3S)_2\}^{8+}$, readily self-assembles from two cofacial $[(TPyP)Fe^{III}(H_2O)_2]$ complexes and four gold clips, $[Au_2(PAnP)Cl_2]$. Under basic conditions, the formation

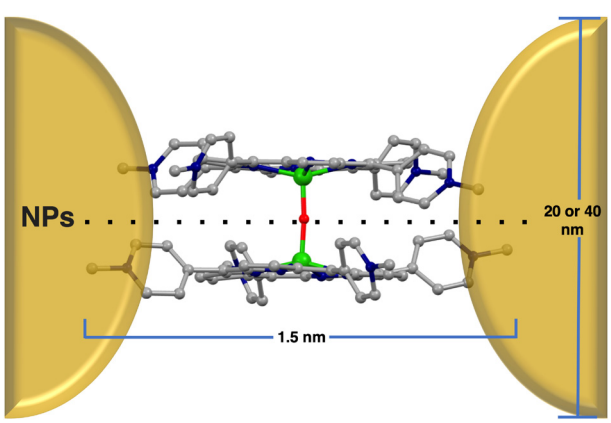

Fig. 7. Plasmonic nanoparticle networks with "edge-on" configuration where the Fe–O–Fe bond of a μ-oxo heme dimer is perpendicular to the interparticle axis of two gold nanoparticles, as reported in [79]

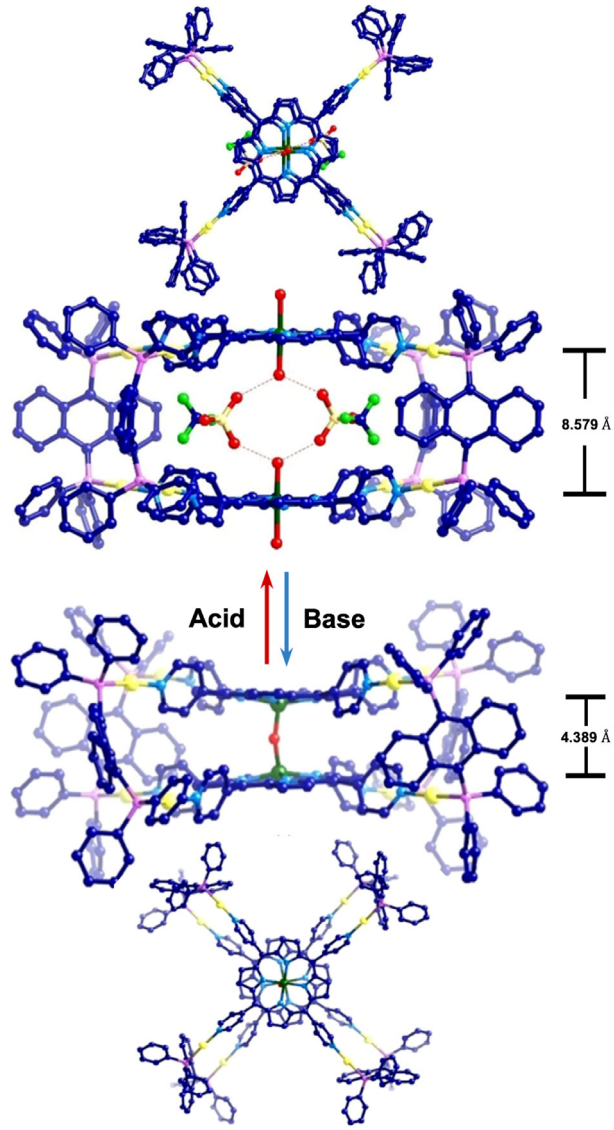

Fig. 8. The pH-responsive molecular cage reversibly undergoes conformational transitions; *e.g.,* the presence of a base promotes the formation of the μ-oxo gold-clip complex, $\{[Au_8(\mu\text{-}PAnP)_4[Fe_2(\mu\text{-}O)(TPyP)_2]\}(CF_3O_3S)_8$, thus inducing contraction of the porphyrin interplane distance. Recreated with permission from [80]. Copyright 2018 John Wiley & Sons, Inc.

of a bridging oxo moiety leads to contraction of the cage and twisting of the two heme cores to minimize the steric hindrance. In the resulting μ-oxo heme dimer, $\{Au_8(\mu\text{-}PAnP)_4[(TPyP)Fe^{III}–O–Fe^{III}(TPyP)]\}^{8+}$, the two ferric heme sites stay tethered by the four gold clips. The formation of the oxo-bridge accompanies significant conformational changes both in the height of the molecular cage (*i.e.,* contraction from 8.6 to 4.4 Å) and the twist angle for the two porphyrin rings (*i.e.,* going from a nearly eclipsed conformation to a bridged structure with a dihedral angle of 20°) [80]. A recent report by Schiemann and coworkers also explained

a new class of μ-oxo heme dimer structures bearing a nitroxide (*i.e.,* stable cyclic radical) pendant arm on each heme core, in which the dynamics of the heme cores and appendages were studied by EPR spectroscopy as well as quantum chemistry based molecular dynamics simulations. The internal structure and dynamics of these μ-oxo heme dimers in solution resemble the motion of a step motor [81].

Other mixed-metal self-assemblies have also been developed using a similar approach where coordination bonds such as metal-pyridyl interactions are employed to assemble highly ordered porphyrin structures. For example, Imamura and coworkers prepared two novel hexaporphyrin constructs through introduction of the two pyridyl groups into the *meso* positions of each porphyrin ring in the μ-oxo heme dimer. Each pyridyl group coordinates to a ruthenium porphyrin unit forming the two hexaporphyrins, $[Ru(OEP)(CO)]_4[Fe(cis\text{-}4\text{-}Py_2T_2P)]_2O$ and $[Ru(OEP)(CO)]_4[Fe(trans\text{-}4\text{-}Py_2T_2P)]_2O$ [82].

Shinkai and coworkers reported another class of modified μ-oxo heme dimers for the boronic-acid-based saccharide recognition. Here, the peripheral boronic acid substituents on the porphyrin rings can act as the sugar-binding sites. Remarkably, these highly selective and sensitive "sugar tweezers" exhibit large association constants (10^4 to 10^5 M^{-1}) with *D*-glucose and *D*-galactose. The saccharide-binding process triggers chiral twisting of the two heme sites which can be readily monitored by circular dichroism (CD) spectroscopy [83, 84].

Further work has also demonstrated that the μ-oxo heme dimers can serve as useful platforms for construction of responsive materials such as dynamic macrocyclic polymers, hydrogels, or ion-sensitive membrane electrodes [85]. These μ-oxo constructs are especially promising for pH sensing due to the ability of the bridging oxo moiety to reversibly undergo protonation and deprotonation, thus bond breakage (*i.e.,* opening process) or formation (*i.e.,* closing process) at various pH values can take place. For example, Deffieux and Schappacher have investigated a reversible unimolecular macrocyclization method (*i.e.,* end-to-end cyclization reaction) using polystyrenes or poly(ethylene oxide)s with terminal ferric heme groups. For the linear ferric precursors, macrocyclization takes place through hydrolysis of ferric heme ends which is followed by intramolecular condensation to form a stable *bis*-iron μ-oxo porphyrin and an assembly of a cyclic polymer ring. The addition of hydrochloric acid to the green cyclic polymer solution, in turn, regenerates the red-brown linear polymer chain with the ferric heme chloride end groups, see Scheme 2 [86, 87]. The authors also explored a reversible on-and-off switching between the linear and cyclic polymer architectures using a redox process. Here, upon exposure to air, the terminal ferrous heme groups of the linear precursor instantly react with O_2 to form the *bis*-iron μ-oxo porphyrin

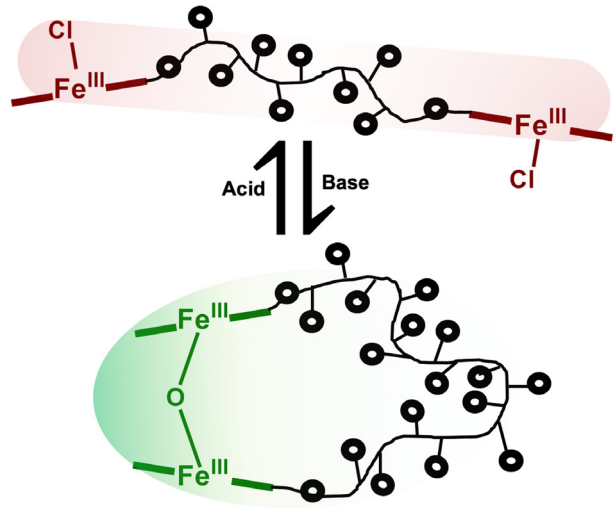

Scheme 2. Reversible on-and-off switching between the linear and cyclic polymer architectures as a function of pH, accompanied by a color change

closing the polymer ring [87]. In another study, a similar approach was extended to the dynamic hydrogels through the incorporation of the terminal ferric heme groups on a 4-arm poly(ethylene oxide) derivative. Hydration of the modified polymer in the presence of a base results in formation of *bis*-iron μ-oxo porphyrins, thus chemical crosslinking and swelling of the gel. Here again, acidification of the hydrogels leads to breakage of the Fe–O–Fe crosslinks that regenerates a dynamic network [88].

Additionally, ultrafine nanorods of the organic-soluble μ-oxo heme dimer, $[(TPP)Fe^{III}–O–Fe^{III}(TPP)]$ [89], and nanocomposites of graphitic carbon nitride sheets modified with the μ-oxo heme dimer (*i.e.,* $[(TPP)Fe^{III}–O–Fe^{III}(TPP)]$-*g*-$C_3N_4$) [90] have been developed as photocatalysts for heterogeneous hydrogen evolution reactions in aqueous media.

Biological relevance. The μ-oxo heme dimer complexes of ferriprotoporphyrin IX have been proven to play critical roles in the molecular mechanism of the chronic infectious gum disease called periodontitis as well as the mechanism of action for antimalarial activity of both quinoline- and non-quinoline-based drugs. The black-pigmented periodontopathogen, *Porphyromonas gingivalis*, is a heme-using bacterium responsible for the adult periodontitis and displays optimum growth at pH = 7.5–8. Several proteins expressed by *P. gingivalis* are engaged in the degradation of the host hemoglobin and final uptake of the ferriprotoporphyrin IX cofactor. Interestingly, Smalley and coworkers have shown that *P. gingivalis* is capable of promoting the formation of μ-oxo heme dimers through various pathways. The stacking of the $[(PPIX)Fe^{III}–O–Fe^{III}(PPIX)]$ complexes through weak π-bonding interactions eventually leads to larger molecular aggregates which deposit on the

bacterial cell surface, protecting *P. gingivalis* against hydrogen peroxide through catalase activity [91, 92].

Several other studies have indicated that the degradation of hemoglobin by the malaria parasite, *Plasmodium falciparum*, also releases the ferriprotoporphyrin IX. The released ferric heme is toxic to *P. falciparum* (*i.e.,* due to the lack of a heme oxygenase pathway in the parasite), so it is mostly detoxified by sequestration into the nontoxic crystalline hemozoin (*i.e.,* the optically dense "malaria pigment" in the infected red blood cells) [93]. A combination of X-ray crystallography, NMR, resonance Raman, Mössbauer, and UV-vis absorption spectroscopies has revealed that antimalarial drugs significantly inhibit the hemozoin crystallization process through the strong "head-on" interactions with the uncrystallized [(PPIX)Fe^{III}–O–Fe^{III}(PPIX)] complexes, see Fig. 9 [94–96]. The large amounts of soluble drug-bound μ-oxo heme dimer adducts oxidatively damage and eventually kill the parasites.

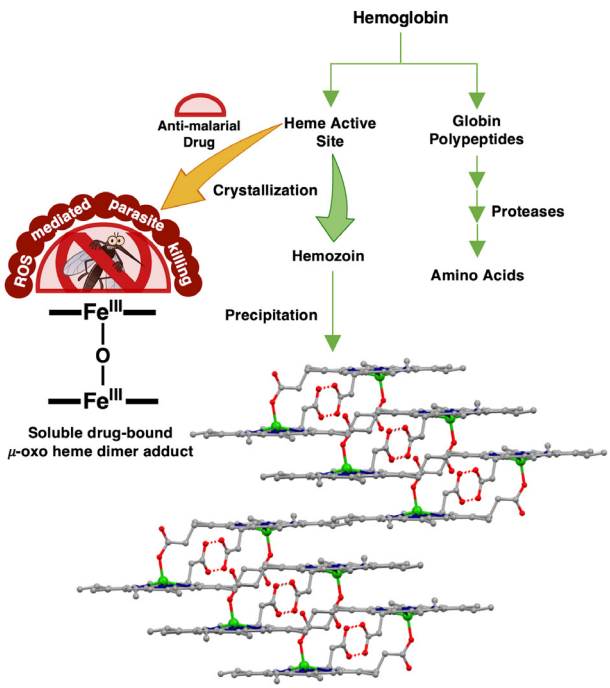

Fig. 9. During hemoglobin degradation in *P. falciparum,* the toxic heme cofactor is released. Thus, the malarial parasite crystallizes the heme to nontoxic hemozoin. An effective antimalarial drug prevents the hemozoin crystallization process through strong "head-on" interactions with the uncrystallized μ-oxo heme dimer (*i.e.,* forming the soluble drug/[(PPIX)Fe^{III}–O–Fe^{III}(PPIX)] adduct) as described in [93]

Oxo-bridged homobinuclear heteroleptic systems: [(P)Fe^{III}–O–Fe^{III}(L)]

The inherent stability of homobinuclear, homoleptic μ-oxo heme complexes, [(P)Fe^{III}–O–Fe^{III}(P)], has been extensively evaluated, *vide supra* [15, 34, 36]. The very same stability that has enabled the synthesis of a plethora of μ-oxo heme dimers imposes a hurdle for the synthesis of homobinuclear, heteroleptic complexes as is evident by the limited examples of this class of constructs. The first novel approach toward the synthesis of an asymmetric *bis*-iron(III)-μ-oxo complex, differing in the metal coordination environment, was employed by WysŁouch and coworkers. The authors reported the first example of an *N*-substituted porphyrin, and thereupon formation of the [(NCH_3TPP)Fe^{III}–O–Fe^{III}(TPP)]$^+$ complex. Methylation of a nitrogen within the porphyrin ring decreases the Fe–O–Fe' angle by about 9° compared to that of the parent μ-oxo complex, [(TPP)Fe^{III}–O–Fe^{III}(TPP)], see Table 1. The interaction between the ferric and methylated nitrogen atom is also weaker than other Fe–N bonds in the [(NCH_3TPP)Fe^{III}–O–Fe^{III}(TPP)]$^+$ complex [97].

The synthesis of another category of the [(P)Fe^{III}–O–Fe^{III}(L)] constructs was inspired by the heme/non-heme diiron core of the nitric oxide reductase (NOR) active site. NOR catalyzes the two-proton, two-electron reduction of two nitric oxide ($NO_{(g)}$) molecules to nitrous oxide (N_2O) and water; this reaction plays a crucial role in bacterial denitrification [98, 99]. The presence of a μ-oxo heme/non-heme diiron center in the fully oxidized state of the NOR active site was confirmed by Moënne-Loccoz and coworkers using resonance Raman and EPR spectroscopies [100–102]. The ligand frameworks for the bioinspired synthetic models of NOR are developed based on the *meso*-substituted porphyrin, F_8TPP, scaffold and the tripodal nitrogen ligand, tris(2-pyridylmethyl)amine (TMPA) that are able to accommodate the heme and non-heme iron sites, respectively. The asymmetric μ-oxo complexes of these NOR synthetic models can be prepared by either acid–base chemistry of the fully oxidized constructs or by reaction of the fully reduced binuclear systems with O_2 [103, 104]. The first example of a synthetic μ-oxo heme/non-heme diiron system was developed by Karlin and coworkers *via* an acid-base self-assembly reaction of the oxidized components, [(F_8TPP)Fe^{III}(OH)] and [(TMPA)$Fe^{III}(Cl)_2$]$^+$, in the presence of a base, forming [(F_8TPP)Fe^{III}–O–Fe^{III}(Cl)(TMPA)]$^+$ [103].

Tethered systems. Two covalently tethered *bis*-Fe(III) μ-oxo heme/non-heme systems, with ^{5}L and later ^{6}L ligand platforms, that are closely related to the parent untethered system, [(F_8TPP)Fe^{III}–O–Fe^{III}(Cl)(TMPA)]$^+$, were also reported by Karlin and coworkers. For [(^{5}L)Fe^{III}–O–Fe^{III}(Cl)]$^+$, the ligand scaffold facilitates intramolecular generation of a μ-oxo bridge between two uniquely coordinated metal sites, see Fig. 10 [103, 105]. Both [(F_8TPP)Fe^{III}–O–Fe^{III}(Cl)(TMPA)]$^+$ and [(^{5}L)Fe^{III}–O–Fe^{III}(Cl)]$^+$ deviate from the near-linear Fe–O–Fe tendencies observed in the related μ-oxo heme dimers. While the [(F_8TPP)Fe^{III}–O–Fe^{III}(F_8TPP)] dimer exhibits an angle of 178°, the Fe–O–Fe' cores in

the untethered and tethered heme/non-heme systems are considerably bent (*i.e.,* 157° and 158°, respectively) [103].

The X-ray crystal structure of the second tethered system, $[(^6L)Fe^{III}–O–Fe^{II}I(Cl)]^+$, much like $[(^5L)Fe^{III}–O–Fe^{III}(Cl)]^+$, reveals an intramolecular bridging Fe–O–Fe' moiety that is less bent (*i.e.,* ⟨Fe–O–Fe' = 167°) than those of the μ-oxo complexes of the ^5L or untethered analogues (Fig. 10) [104]. Here, the length of the linker and anchoring location to the pyridyl ring of the non-heme site directly dictates the flexibility of the tethered non-heme iron chelate and the degree to which the Fe–O–Fe' moiety bends.

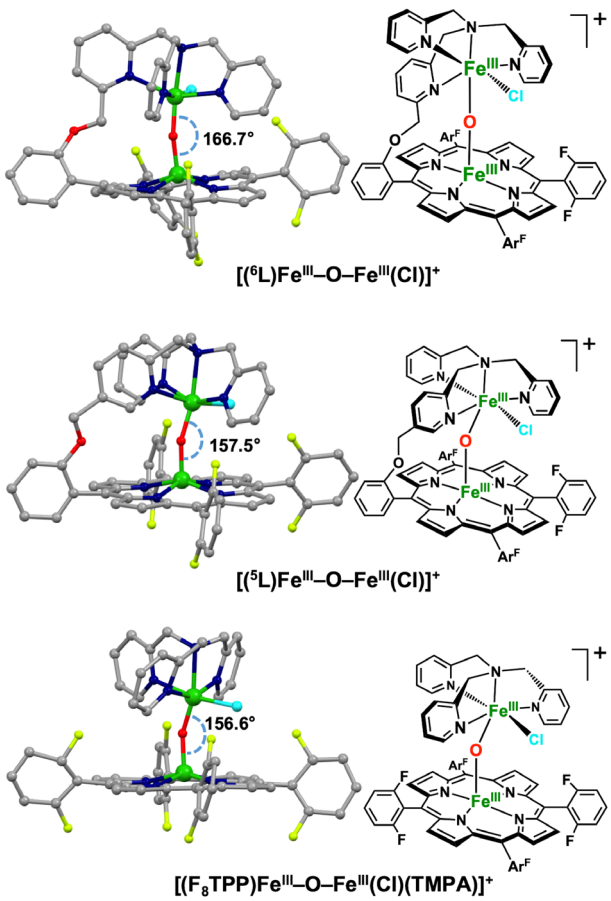

Fig. 10. Structures of tethered and untethered synthetic μ-oxo heme/non-heme diiron complexes discussed in this review

Catalysis. Later, Karlin, Meyer and coworkers investigated the photophysics of $[(^6L)Fe^{III}–O–Fe^{III}(Cl)]^+$ for both stoichiometric and catalytic oxidation of substrates. Anaerobic and aerobic conditions were probed and the transfer of the bridging oxo ligand to various substrates was investigated by ^{18}O-labeling experiments. Under an anaerobic condition, with a suitable substrate present, the photodisproportionation can take place to generate the proposed transient intermediates, $[(^6L)Fe^{IV}=O...Fe^{II}(Cl)]$ or $[(^6L)Fe^{II}...O=Fe^{IV}(Cl)]$, followed by oxidation of the substrate and formation of the reduced diiron complex, $[(^6L)Fe^{II}...Fe^{II}(Cl)]^+$. In turn, the intermediates can readily undergo recombination to regenerate the starting μ-oxo complex, $[(^6L)Fe^{III}–O–Fe^{III}(Cl)]^+$, when no substrate is available for the oxygen transfer (OAT). In benzene, oxygen atom transfer does not occur without an exogenous substrate such as triphenylphosphine, since the very strong C–H bonds in benzene are not reactive enough toward photooxidation by the heme/non-heme complex. By contrast, toluene and tetrahydrofuran (THF) both enable the photoreduction of $[(^6L)Fe^{III}–O–Fe^{III}(Cl)]^+$ to $[(^6L)Fe^{II}...Fe^{II}(Cl)]^+$ as both contain more reactive C–H bonds than those found in benzene. Here, the transiently formed ferryl-oxo species homolytically cleaves the C–H bond of toluene or THF. Exposing these OAT reactions to the air regenerates the μ-oxo complex from the reduced form, $[(^6L)Fe^{II}...Fe^{II}(Cl)]^+$. The newly reformed $[(^6L)Fe^{III}–O–Fe^{III}(Cl)]^+$ complex thus serves as a catalyst for the continued oxidation of triphenylphosphine, toluene, or THF [106].

Additionally, $[(^6L)Fe^{III}–O–Fe^{III}(Cl)]^+$ was subjected to neat chlorinated substrates (*e.g.,* 1,2-dichlorobenzene and chlorobenzene) and exogenous chlorinated substrates (*e.g.,* benzyl chloride) in benzene. Upon photolysis, the aromatic C–Cl bond cleavage reactions proceed to form biphenyl trichlorides or biphenyl monochlorides from dichlorobenzene and chlorobenzene, respectively, while the photochemical oxidative dechlorination of the benzylic C–Cl bond in benzyl chloride leads to the formation of benzaldehyde in 70% yield. After initial dechlorination, however, the fully oxidized μ-oxo heme/non-heme complex was not regenerated; instead, the chlorinated complex, $\{[(^6L)Fe^{III}(Cl)...Fe^{III}(Cl)]_2O\}^{2+}$, involving two tethered systems with a heme/non-heme bridging oxo was formed and characterized *via* UV-vis spectroscopy and electron spray ionization mass spectrometry (ESI-MS) [106]. The "additional" chloride ligand in the complex compared to the starting μ-oxo compound is derived from the substrates and hinders the reformation of the parent $[(^6L)Fe^{III}–O–Fe^{III}(Cl)]^+$ complex under aerobic conditions [106].

Recently, a *bis*-iron(III) μ-oxo porphyrin/phthalocyanine (P/Pc) complex, $[(P)Fe^{III}–O–Fe^{III}(Pc)]$, has been shown to catalyze the reduction of O_2 to water. To increase the efficiency of O_2 reduction, iron cores and highly flexible linkers were both incorporated into the ligand scaffold, see Fig. 11. The formation of the μ-oxo complex was corroborated by both EXAFS and DFT studies, supporting the presence of a greatly bent Fe–O–Fe moiety (146°); furthermore, fitting of Fe K-edge EXAFS data gave Fe–O and Fe–Fe distances of 1.81 and 3.47 Å, respectively, both of which were slightly elongated compared to those of the corresponding μ-oxo heme dimer. Electrochemical studies were conducted on the μ-oxo phthalocyanine/porphyrin complex as well as the corresponding *bis*-iron(III) μ-oxo porphyrin and phthalocyanine dimers. The onset potentials for O_2

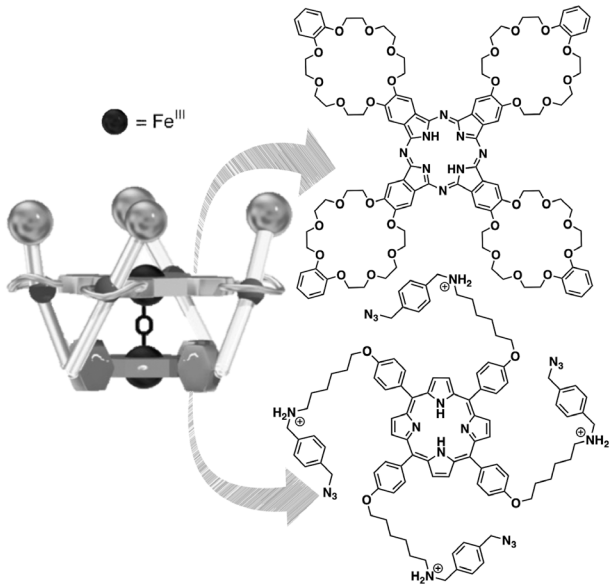

Fig. 11. Structure of the homobinuclear, heteroleptic *bis*-iron(III) μ-oxo porphyrin/phthalocyanine complex. Adopted with permission from [107]. Copyright 2017 John Wiley & Sons, Inc.

reduction (E_o *vs*. a reversible hydrogen electrode (RHE)) were reported as increasingly positive in the order of: [(P)Fe^{III}–O–Fe^{III}(P)] (E_o = 0.59 V) < [(Pc)Fe^{III}–O–Fe^{III}(Pc)] (E_o = 0.68 V) < [(P)Fe^{III}–O–Fe^{III}(Pc)] (E_o = 0.78 V). The *bis*-iron(III) μ-oxo porphyrin/phthalocyanine complex clearly exhibits the lowest overpotential compared to its homobinuclear, homoleptic counterparts. After quantification of O_2 electroreduction products (*e.g.,* H_2O and H_2O_2), it was determined that the four-electron reduction of O_2 to water (*i.e.,* with the yield of 88%) was the primary reaction catalyzed by the [(Pc)Fe^{III}–O–Fe^{III}(Pc)] complex, selectively [107].

Oxo-bridged heterobinuclear heteroleptic systems: [(P)Fe^{III}–O–M(L)]$^{n+}$

Further interesting progress in the field of heme chemistry includes the development of a class of oxo-bridged, heterobinuclear complexes bearing a copper site in addition to the heme core, [(P)Fe^{III}–O–Cu^{II}(L)]$^+$. Such complexes are broadly embraced as synthetic models for the active site of cytochrome *c* oxidase in which heme-a_3 and Cu_B are adjacent to one another. As a crucial component of the electron transport chain, C*c*O catalyzes the four electron, four proton reduction of dioxygen to water and simultaneously generates the electrochemical gradient across the membrane, necessary for ATP production [108–110]. Karlin and coworkers have done significant work on synthetic heme/Cu models over the years and demonstrated that the related μ-oxo heme/Cu complexes can be prepared by dioxygen or acid–base chemistry [111–113].

The first example of such μ-oxo complexes was [(F_8TPP)Fe^{III}–O–Cu^{II}(TMPA)]$^+$, which was obtained from the reaction of an equimolar mixture of the [(F_8TPP)Fe^{II}] and [(TMPA)Cu^{I}(MeCN)]$^+$ complexes with O_2 at room temperature. Interestingly, despite the known substantial thermodynamic stability of the μ-oxo iron dimer, [(P)Fe^{III}–O–Fe^{III}(P)], the kinetically stable μ-oxo heme/Cu complexes, [(P)Fe^{III}–O–Cu^{II}(L)]$^+$, are formed. Here, the bridging oxo moiety is derived from O_2 *via* fast thermal disproportionation of a binuclear peroxide intermediate (*i.e.*, [(P)Fe^{III}–(O_2^{2-})–Cu^{II}(L)]$^+$) at room temperature, with the concomitant release of half of an equivalent of O_2 [108, 114]. One exception has been reported for synthesis of [(TMP)Fe^{III}–O–Cu^{II}(5MeTPA)]$^+$ where the μ-peroxo complex remains stable for several months; over an extended period of time, it only very slowly converts to its μ-oxo counterpart [115]. Later, it was shown that [(P)Fe^{III}–O–Cu^{II}(L)]$^+$ can also be formed *via* mixing [(P)Fe^{III}(OH)] and [(L)Cu^{II}]$^{2+}$ species [108] or alternatively [(P)Fe^{III}] and [(L)Cu^{II}(OH)]$^+$ species [109] in the presence of a base.

Furthermore, X-ray crystallography and Fe and Cu-edge EXAFS studies on the reported [(P)Fe^{III}–O–Cu^{II}(L)]$^+$ complexes with the tripodal tetradentate chelates indicated a near-linear Fe–O–Cu arrangement. Mössbauer, EPR, and magnetic susceptibility studies also revealed the strong antiferromagnetic coupling of the high-spin Fe^{III} ($S = {}^5/_2$) and Cu^{II} ($S = {}^1/_2$) sites through the μ-oxo moiety, rendering an overall spin state of S = 2 [108, 109]. The μ-oxo heme/Cu complexes also exhibit the very distinctive red-shifted Soret absorption bands (*i.e.*, λ_{max} ~435–455 nm, see Table 1) compared to those of classical high-spin ferric hemes. The weaker affinity of Cu(II) for the bridging oxo, and therefore the greater degree of π charge donation available onto the ferric center by the oxo group, is likely responsible for the characteristic red-shift.

The bridging oxo moiety can be reversibly protonated to give the corresponding μ-hydroxo complex, [(P)Fe^{III}–(OH)–Cu^{II}(L)]$^+$, and with protonation, bending of the Fe–O(H)–Cu moiety and lengthening of the Fe^{III}–O(H) and Cu^{II}–O(H) bonds occurs, which consequently lowers the degree to which the iron atom is pulled out of the porphyrin plane [108, 116, 117]. Holm and coworkers reported the only crystal structure of a μ-hydroxo heme/Cu complex utilizing the OEP framework (*i.e.,* [(OEP)Fe^{III}–(OH)–Cu^{II}(Me_5dien)($OClO_3$)]$^+$) [118]. In this complex, the Fe–(OH)–Cu angle is about 157° which is significantly more bent compared to the Fe–O–Cu angle (*i.e.*, 177°) in the related μ-oxo heme/Cu complex based on the OEP scaffold, [(OEP)Fe^{III}–O–Cu^{II}(Me_6tren)]$^+$ [108, 118]. Note, however, that the cupric ligations in these complexes are significantly different from one another. A similar degree of bending was reported for the protonation of [(F_8TPP)Fe^{III}–O–Cu^{II}(TMPA)]$^+$, wherein the Fe–O–Cu moiety approaches linearity (*i.e.,* 178°) [119] and the

Fe–(OH)–Cu moiety is significantly more bent (*i.e.*, 157°) as confirmed by EXAFS [116].

Markedly, studies by Karlin and coworkers have revealed that changes in the coordination environment of the cupric site, tridentate *vs*. tetradentate ligands, can dramatically influence both μ-oxo heme/Cu physical properties and reactivity [113, 120]. Changing tripodal tetradentate chelates (*e.g.,* TMPA, Me_6tren, or Me_5dien) bound to the cupric center to tridentate ligands (*e.g.,* L^{Me2N}, MePY2, AN) results in significant bending (*i.e.,* ⟨Fe–O–Cu is 142–150°) and elevated basicity of the bridging oxo group. As discussed earlier, bending upon protonation can be explained by varying degrees of re-hybridization at the bridging oxygen atom, with the extreme case being a change from *sp* in a perfectly linear μ-oxo compound to sp^2 in a very bent μ-hydroxo complex with an angle of 120°. Consequently, protonation of the bridging oxo moieties requires varying degrees of geometric and electronic rearrangements as explained by Norton and coworkers; thus, the extent of the overall re-hybridizations can directly dictate the kinetics of the protonation reactions [11, 121].

The proton transfer chemistry of an oxo-bridged heterometallic heme/Cu complex and the corresponding μ-hydroxo complex has been a matter of great importance for understanding the function of the C*c*O active site. Karlin and coworkers have thus determined the pK_a of the bridging hydroxo moiety through acid–base titration experiments in some of the synthetic $[(P)Fe^{III}–O–Cu^{II}(L)]^+$ systems, such as $[(F_8TPP)Fe^{III}–O–Cu^{II}(TMPA)]^+$ (Chart 2) [116] and $[(F_8TPP)Fe^{III}–O–Cu^{II}(MePY2)]^+$ (Chart 2) [122]. The tridentate cupric core in the latter resulted in a slightly more basic oxo bridge ($16.7 < pK_a < 17.6$ in CH_3CN; aqueous $pK_a \cong 9.6$) compared to that of the former bearing the tetradentate cupric site ($14 < pK_a < 17$ in CH_3CN; aqueous $pK_a \cong 8$). A comparison of the Fe–O–Cu angles shows that the μ-oxo complex of $[(F_8TPP)Fe^{III}–O–Cu^{II}(TMPA)]^+$ is nearly straight (178°) while that of $[(F_8TPP)Fe^{III}–O–Cu^{II}(MePY2)]^+$ is significantly bent (142°), further illustrating the aforementioned observation that as the Fe–O–Cu core becomes more bent, the bridging oxo moiety becomes more basic. However, the linearity of the Fe–O–Cu core is not the only factor defining the basicity: the $[(F_8TPP)Fe^{III}–O–Cu^{II}(AN)]^+$ with a larger Fe–O–Cu core (*i.e.,* 150°) exhibits more basicity, with estimated aqueous pK_a of 10.5, than $[(F_8TPP)Fe^{III}–O–Cu^{II}(MePY2)]$ with a more bent Fe–O–Cu core (*i.e.,* 142°) [123, 124].

Tethered systems. Karlin and coworkers have also prepared several other ligand platforms for the formation of synthetic μ-oxo heme/Cu complexes. Two of these platforms are porphyrins bearing covalently tethered tetradentate copper chelates, ^{6}L and ^{5}L, which were discussed under the previous class of oxo-bridged heme complexes, *i.e*., oxo-bridged homobinuclear heteroleptic systems. Chart 2 depicts the crystal structures of the untethered $[(F_8TPP)Fe^{III}–O–Cu^{II}(TMPA)]^+$ as well as its tethered analogues, *i.e*., $[(^5L)Fe^{III}–O–Cu^{II}]^+$ and $[(^6L)Fe^{III}–O–Cu^{II}]^+$ [110]. The μ-oxo heme/Cu complex of the ^{5}L scaffold possesses a very bent Fe–O–Cu core with an angle of ~141°, due to the ligand constraints imposed by the linker. This bent geometry can translate to partial sp^2 orbital hybridization of the bridging oxo moiety, which can consequently facilitate a faster and more facile protonation process to form the μ-hydroxo complex upon the addition of an acid. The addition of 1 equivalent of a weak acid such as *N*-methylmorpholinium triflate with pK_a of 16.6 in acetonitrile does not result in protonation of the untethered $[(F_8TPP)Fe^{III}–O–Cu^{II}(TMPA)]^+$ complex, while the same acid reacts with both tethered systems generating the bridging hydroxo species for the ^{6}L platform, $[(^6L)Fe^{III}–(OH)–Cu^{II}]^{2+}$ and resulting in cleavage of the oxo bridge for the more strained ^{5}L platform to form $[(^5L)Fe^{III}–(OH)...Cu^{II}(CF_3O_3S)]^+$ [123]. Therefore, the μ-oxo moiety in $[(^6L)Fe^{III}–(OH)–Cu^{II}]^+$ or $[(^5L)Fe^{III}–O–Cu^{II}]^+$ is more basic than that in $[(F_8TPP)Fe^{III}–O–Cu^{II}(TMPA)]^+$, and a μ-hydroxo species appears inaccessible in $[(^5L)Fe^{III}–O–Cu^{II}]^+$.

Another interesting structural observation for $[(P)Fe^{III}–(O_2^{2-})–Cu^{II}(L)]^+$, with L being the tetradentate TMPA chelate, is seen when comparing the ligand arrangements around the cupric centers in the parent complex, $[(F_8TPP)Fe^{III}–O–Cu^{II}(TMPA)]^+$ and its closely related analogue $[(TMPP)Fe^{III}–O–Cu^{II}(TMPA)]^+$, in which only the identity of the peripheral substituents on the porphyrin ring varies. Despite the fact that both complexes possess similar Fe–O–Cu core angles and identical cupric chelate, the copper centers adopt very different geometries. The TMPA-copper ligation, for the $[(TMPP)Fe^{III}–O–Cu^{II}(TMPA)]^+$ complex, occurs within a nearly perfect trigonal bipyramidal (TBP) geometry ($\tau = 0.9$), while for the $[(F_8TPP)Fe^{III}–O–Cu^{II}(TMPA)]^+$ construct, the copper ligand is sterically hindered due to the presence of the sizeable fluorine atoms projecting off the phenyl groups, thus the cupric center adjusts to a distorted square pyramidal (SP) coordination ($\tau = 0.3$) [108, 125].

Notably, $[(^6L)Fe^{III}–O–Cu^{II}]^+$ has a slightly more TBP-like configuration ($\tau = 0.5$) than its untethered analogue, *i.e*., $[(F_8TPP)Fe^{III}–O–Cu^{II}(TMPA)]^+$. Given that the cupric ligand is attached to an aromatic ring on the *meso* position of the ferric heme, the two free pyridyl arms settle into a different spatial arrangement than those within the untethered heme/Cu complex, see Chart 2.

Reactivity toward nitric oxide. Nitric oxide ($NO_{(g)}$) plays a critical role as a versatile signaling molecule in living organisms and can be generated through two unique pathways that are intimately dependent on physiological fluctuations in O_2 concentrations. The production of $NO_{(g)}$ takes place *via* the nitric oxide synthase (NOS) pathway, requiring L-arginine, during normoxic conditions; hence the added O_2 requirement for this pathway. An alternate pathway for $NO_{(g)}$ generation, required under low O_2

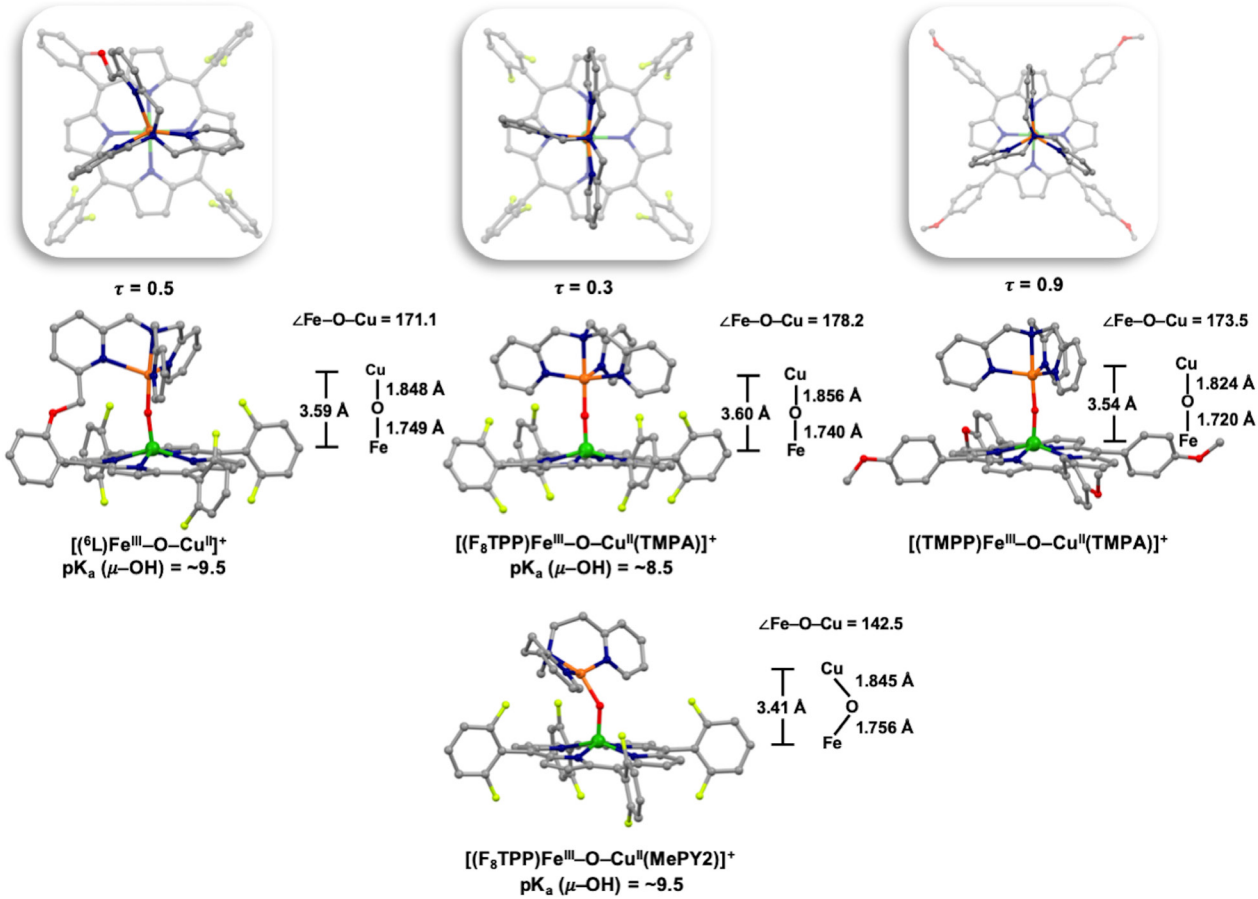

Chart 2. Molecular structures of μ-oxo heme/Cu complexes reported by Karlin and coworkers. Presented pK_a values are calculated for aqueous media using the estimate that the measured pK_a values in acetonitrile are 7.5 ± 1 unites larger than in water

concentrations (*i.e.*, hypoxic conditions) and those associated with cellular stress, is an enzymatic reduction of nitrite deemed to be important in the modulation of mitochondrial respiration [126].

Previous studies demonstrated that C*c*O is capable of nitrite reduction when exposed to hypoxic conditions [127]. Consequently, the initial report by Karlin and coworkers introduced a synthetic heme/Cu assembly mediating the redox interplay between nitrite and $NO_{(g)}$ [128]. Further studies revealed that the partially reduced form of the heme/Cu assembly facilitates nitrite reduction to $NO_{(g)}$ and the cupric center serves as a Lewis acid directing the nitrite ion to bind to the ferrous heme center through *N*-atom coordination. Additionally, the cupric site facilitates the nitrite (N–O) bond cleavage while the ferrous heme provides the reducing electron [129]. Interestingly, in turn the fully oxidized form of the same assembly as a μ-oxo heme/Cu complex could oxidize $NO_{(g)}$ back to nitrite. $NO_{(g)}$ oxidation to nitrite was accomplished through the addition of two equivalents of $NO_{(g)}$ to one equivalent of the fully oxidized the parent $[(F_8TPP)Fe^{III}–O–Cu^{II}(TMPA)]^+$ complex to yield $[(F_8TPP)Fe^{II}(NO)]$ and $[(TMPA)Cu^{II}(NO_2)]^+$ [128].

Further studies involved similar μ-oxo heme/Cu complexes with variation among the copper ligand framework. These complexes included $[(F_8TPP)Fe^{III}–O–Cu^{II}(AN)]^+$ and $[(F_8TPP)Fe^{III}–O–Cu^{II}(MePY2)]^+$. Tridentate ligands around the copper center gave similar results to those obtained with the tetradentate ligand TMPA, however, with an increase in reactivity. Alterations in copper-ligand denticity and electronics modulate the reactivity of the μ-oxo heme/Cu complexes toward $NO_{(g)}$. This is perhaps achieved through regulating the steric hindrance and electronic environment surrounding the copper center and, thus tuning the basicity and accessibility of the bridging oxo moiety. Remarkably, a higher degree of bending, basicity, and accessibility of the bridging oxo moiety results in an increase in $NO_{(g)}$ oxidase reactivity.

In order to further comprehend $NO_{(g)}$ reactivity with the μ-oxo heme/Cu complexes, the parent porphyrin ligand F_8TPP was replaced by a more electron rich analogue, TMPP, bearing strong electron-donating peripheral groups. The addition of $NO_{(g)}$ to $[(TMPP)Fe^{III}–O–Cu^{II}(TMPA)]^+$ enables the detection of an intermediate (Scheme 3, *bis*-NO intermediate) through UV-vis monitoring at -20 °C [125]. This intermediate

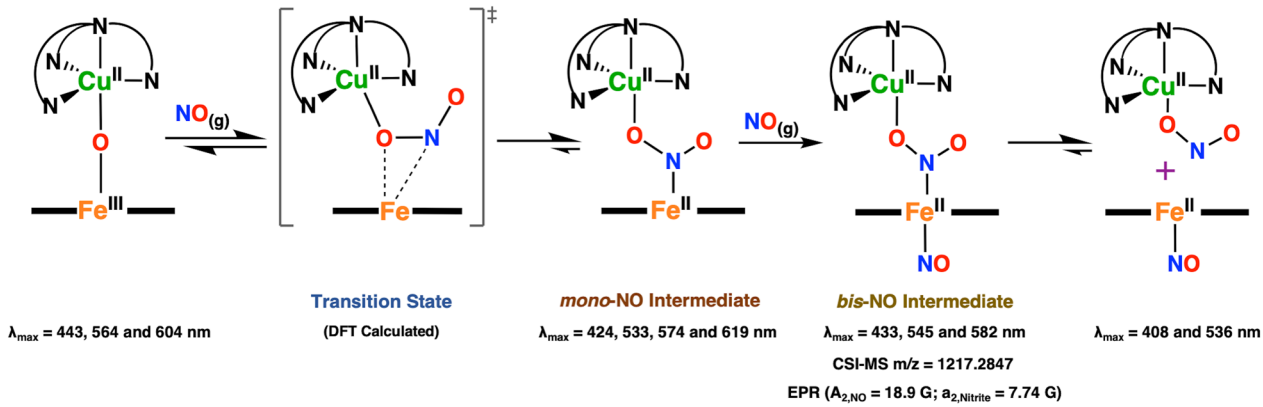

Scheme 3. Proposed reaction mechanism for $NO_{(g)}$ oxidase chemistry mediated by μ-oxo heme/Cu assemblies, $[(P)Fe^{III}–O–Cu^{II}(L)]^+$, producing observed products. Adapted with permission from [125]. Copyright 2015 American Chemical Society

isosbestically converts to the final products, $(TMPP)Fe^{II}(NO)$ and $[(TMPA)Cu^{II}(NO_2)]^+$, in a first-order process with rate constant $k_{dissoc.} = 6.7 \times 10^{-3}$ s^{-1} at -20 °C.

Guided by DFT calculations (*i.e.*, proposing that the observed *bis*-NO intermediate is a ferrous species), $[(TMPA)Cu^{II}(NO_2)]^+$ was mixed with $[(TMPP)Fe^{II}(NO)]$ at -125 °C to determine if a nitrite anion, as bound to a cupric site, could bind to a ferrous-nitrosyl complex. Cooling of the mixture resulted in a new UV-vis spectrum identical to that of the *bis*-NO intermediate, supporting that the *bis*-NO species comprises a six-coordinate ferrous heme-nitrosyl species joined to a cupric nitrite entity through the nitrogen atom of the bridging nitrite. The exact nature of this intermediate was also confirmed by low-temperature stopped-flow kinetic and EPR spectroscopies as well as cryo-spray ionization mass spectrometry (CSI-MS) at -60 °C (see Scheme 3). Furthermore, the reaction proved to be reversible as temperatures rose.

An initial transition state was proposed by DFT calculations in which the formation of a three-membered chelate ring between the iron, bridging oxo, and the nitrogen (N) atom of the $NO_{(g)}$ is observed (transition state, Scheme 3). Formation of this "triangular" structure happens *via* the electrophilic attack of the initial $NO_{(g)}$ molecule, followed by electron transfer from $NO_{(g)}$ to the ferric heme. The experimentally observed low activation enthalpy and negative activation entropy derived from the kinetic studies also support this sequence of events [125]. A *mono*-NO adduct in which there is a *N*-bound nitrite to the resulting ferrous heme and an oxygen atom bound to the cupric center is the first intermediate. This finding is of significant relevance to C*c*O as a similar ferrous heme–nitro species has been detected in the heme/Cu active-site of the enzyme by resonance Raman spectroscopy.

To generate the second intermediate, a second $NO_{(g)}$ molecule attacks the ferrous heme, resulting in the aforementioned *bis*-NO adduct. The second $NO_{(g)}$ is not involved in the redox chemistry and only traps the ferrous heme formed during the prior step to generate a stable ferrous heme nitrosyl product. Remarkably, the binding of the second $NO_{(g)}$ is irreversible, and addition of the first $NO_{(g)}$ to μ-oxo heme/Cu complex, $[(TMPP)Fe^{III}–O–Cu^{II}(TMPA)]^+$ is about an order of magnitude faster than the irreversible binding of the second $NO_{(g)}$ [113, 125].

Further broadening the scope of oxo-bridged heterobinuclear heteroleptic systems points to complexes in which the non-iron metal center is composed of either Cr or Co. The first oxo-bridged heme/Cr complex crystal structure was deposited by West and coworkers for $[(TMPP)Fe^{III}–O–Cr^{III}(Py)(TPP)]$ [130]. Later, Tsuchida and coworkers crystallized another complex, $[(TPP)Fe^{III}–O–Cr^{III}(Pip)(TPP)]$, which closely resembles the former $[(P)Fe^{III}–O–Cr^{III}(P')(L)]^+$ [131]. Exchanging the TMPP ligand for a second TPP had little effect on the Fe–O–Cr moiety, both having a near-linear angle of about 178°, see Table 1; however, the twist angle between the two porphyrins slightly decreases in $[(TPP)Fe^{III}–O–Cr^{III}(Pip)(TPP)]$ as opposed to that of $[(TMPP)Fe^{III}–O–Cr^{III}(Py)(TPP)]$ (*i.e.*, 30° and 32°, respectively), perhaps as a subtle measure to decrease the interaction between the phenyl groups of the heme and the phenyl groups of the chromium-bound porphyrin. The observed change in the twist angle is due to shorter the Fe–M distance for $[(TPP)Fe^{III}–O–Cr^{III}(Pip)(TPP)]$ than that of $[(TMPP)Fe^{III}–O–Cr^{III}(Py)(TPP)]$ (*i.e.,* 3.53 and 3.60 Å, respectively) and in part is a consequence of the varying nature of the axial ligands binding to the chromic cores. As expected, the $[(P)Fe^{III}–O–Cr^{III}(P')(L)]^+$ complexes exhibit considerable antiferromagnetic coupling between Cr(III) ($S = {}^3/_2$) and Fe(III) ($S = {}^5/_2$) consistent with an assignment of 1 as an $S = 1$ electronic ground state species.

In addition to $[(P)Fe^{III}–O–Cr^{III}(P')(L)]^+$ complexes, one oxo-bridged crystal structure involving a cobalt core instead of a chromium site has been reported by Karlin and coworkers, that of $[(F_8TPP)Fe^{III}–O–Co^{II}(TMPA)]^+$ [132]. While O_2 chemistry with the parent

$[(F_8TPP)Fe^{III}–O–Cu^{II}(TMPA)]^+$ complex gave a peroxo-bridged heme/Cu complex, identification of a peroxo-bridged heme/Co complex was not possible. Furthermore, there is a greater degree of bending in the Fe–O–M moiety than that of in the parent complex, $[(F_8TPP)Fe^{III}–O–Cu^{II}(TMPA)]^+$ (*i.e.,* ⟨Fe–O–Co is 172° and ⟨Fe–O–Cu is 178°, respectively). Lastly, the Fe–O distance for $[(F_8TPP)Fe^{III}–O–Co^{II}(TMPA)]^+$ (1.75 Å) is between those of the parent compounds, $[(F_8TPP)Fe^{III}–O–Cu^{II}(TMPA)]^+$ (1.74 Å) and $[(F_8TPP)Fe^{III}–O–Fe^{III}(TMPA)]^+$, (1.78 Å) and the Co core adopts a trigonal bipyramidal surrounding while the cupric center in the parent complex accommodates a distorted square pyramidal geometry.

Rezzano and coworkers have also reported iron/copper porphyrin-based nanostructures with the positively and negatively charged porphyrins for sensor application. The J-aggregates of those porphyrins are stabilized by Fe–O–Cu bonds, electrostatic forces, and π-stacking interactions. The Raman features of these supramolecular assemblies can be used for sensing a variety of species such as H_2O_2, NO_2^-, SO_3^{2-}, and N_3^-. The authors proposed that the putative $[(T_4PyP)Fe^{III}–O–Cu^{II}(T_4PyP)]^{7+}$ units are stacked by the neighboring $[H_4TPPS]^{2-}$ complexes [133]. The proposed $[(P)Fe^{III}–O–Cu^{II}(P)]^{n+}$ complex would be the only example of an oxo-bridged heterobinuclear homoleptic system.

CONCLUSION

From the results presented herein, it is evident that the chemistry of (hydr)oxo-bridged heme complexes spans studies in synthetic inorganic chemistry, biology, materials science, energy and environmental sciences. In order to develop a detailed understanding of their structure-function relationships, it is necessary to integrate perspectives and techniques from all subdisciplines. We have highlighted the recent progress and contributions in synthesis, structural and spectroscopic investigations, and reactivity and catalytic studies of a variety of (hydr)oxo-bridged heme constructs. The wealth of (hydr)oxo-bridged binuclear structures in the Cambridge Structural Database, and detailed studies of the functions and properties of these assemblies explain the increasing prevalence of (hydr)oxo-bridged heme constructs in a very wide range of industrial applications such as homogenous or heterogenous catalysis, sensing, optoelectronics, and healthcare-related uses.

As we point out, the properties and reactivity of the bridging (hydr)oxo moieties are controlled by the coordination environment of the heme core, the nature of the second metal center attached to the (hydr)oxo group and its and chelating scaffold, and the flexibility or rigidity of the entire framework. Further investigations and deeper understanding of the properties and reactivities of these (hydr)oxo-bridged heme constructs are likely to improve their performance and may uncover many additional applications.

Acknowledgments

We gratefully acknowledge the University of North Carolina at Greensboro for the financial support provided in the form of startup funds. We are also thankful for the support and services rendered by the faculty and staff of the Department of Chemistry and Biochemistry.

ABBREVIATIONS

TPP:	tetraphenylporphyrin
Porphen:	(5,10-(1,10-phenanthroline-2,9-diyl)-*bis*(4-phenylene-2-phenyl) porphyrinato)
$TPPBr_4$:	(2,3,12,13-tetrabromo-5,10,15,20-tetraphenylporphyrinato
TTP:	*meso*-tetrakis(*p*-tolyl-porphyrinato)
TMPyP:	tetrakis(1-methylpyridinium-4-yl) porphyrinato
TPPS:	tetrakis(4-sulfonatophenyl)porphyrinato
p-CTPP:	(5,10,15,20-tetra(4-chlorophenyl) porphyrinato
TBPP:	tetrakis(*p*-bromophenyl-porphyrinato
FF:	Face-to-Face *aka* 5-(*o*-aminophenyl)-10,15,20-triphenylporphyrin
$TPPF_5$:	(5,10,15,20-tetrakispentafluorophenyl) porphyrinato
F_8TPP:	tetrakis(2,6-difluorophenyl)porphyrinate
OC_2OPor:	four-atom-linked capped porphyrin
OEP:	2,3,7,8,12,13,17,18-octaethylporphyrinato
trans-4-Py_2T_2:	5,15-di(4-pyridyl)-10,20-ditolylporphyrinato
cis-4-Py_2T_2:	5,10-di(4-pyridyl)-15,20-ditolylporphyrinato
DEsP:	diester porphyrin
ODM:	5,15-dimethyl-2,3,7,8,12,13,17,18-octaethylporphyrin
TCPP:	*meso*-tetra(4-carboxyphenyl)porphyrin
din-OEP:	5,10-dinitrooctaethylporphyrin or 5,15-dinitrooctaethylporphyrin

trn-OEP:	5,10,15-trinitrooctaethylporphyrin
tn-OEP:	5,10,15,20-tetranitrooctaethylporphyrin
PPIXDME:	protoporphyrin IX dimethyl ester
DEP:	diethylpyrrole-bridged *bis*-porphyrin
ETA:	ethane-linked μ-oxo *bis*-octaethylporphyrin
ETE:	1,2-*bis*(2,3,7,8,12,13,17,18-octaethylporphyrinnyl)ethene
DPD:	(dibenzofuran-2,9-diyl)-*bis*((3,8,12,17-tetraethyl-2,7,13,18-tetramethylporphyrinato
DPA:	2,8,13,17-tetraethyl-3,7,12,18-tetramethylporphyrin-5-yl)anthracene
DPX:	2,8,13,17-tetraethyl-3,7,12,18-tetramethylporphyrin-5-yl)-9,9-dimethylxanthene
^{6}L:	5-(*o*-O-[(*N*,*N*-*bis*(2-pyridylmethyl)-2-(6-methoxyl)pyridinemethanamine) phenyl]-10,15,20-tris(2,6-difluorophenyl)porphine
^{5}L:	α,β,γ-tris(2,6-Difluorophenyl)-δ-(((2-(*bis*(2-pyridylmethyl)amino) methyl-5-pyridyl)methoxy)phenyl) porphyrinato
TMPA:	*tris*(2-pyridylmethyl)amine
NCH_3TPP:	*N*-methyl-5,10,15,20-tetraphenylporphyrinato
TMP-5MeTPA:	10,15,20-*tris*(2,4,6-trimethylphenyl)-5-(2′-*bis*((5″-methyl-2″-pyridylmethyl) aminomethyl)pyridine-5′-carboxylic-aminophenyl)porphyrinate(2-)
MePY2:	*bis*(2-pyridyl-ethyl)methylamine
L^{Me2N}:	*N*,*N*-*bis*{2-[2-(*N*′,*N*′-4-dimethylamino) pyridyl]ethyl}methylamine)
AN:	3,3′-imino-*bis*(*N*,*N*-dimethylpropylamine)
Me_6tren:	*tris*[(*N*,*N*-dimethylamino)-ethyl]amine
Me_5dien:	1,1,4,7,7-pentamethyldiethylenetriamine
PAnP:	9,10-*bis*(di-phenylphosphino)anthracene
TPyP:	*meso*-tetra(4-pyridyl)-porphyrinato
P:	porphyrinate dianion
Pc:	phthalocyaninate dianion

REFERENCES

1. Poulos TL. *Chem. Rev.* 2014; **114**: 3919–3962.
2. Dawson J. *Science* 1988; **240**: 433–439.
3. Chin D-H, La Mar GN and Balch AL. *J. Am. Chem. Soc.* 1980; **102**: 4344–4350.
4. Fleischer EB and Srivastava TS. *J. Am. Chem. Soc.* 1969; **91**: 2403–2405.
5. Hoffman AB, Collins DM, Day VW, Fleischer EB, Srivastava TS and Hoard JL. *J. Am. Chem. Soc.* 1972; **94**: 3620–3626.
6. In addition to the initial reports mentioned in this review, other structural data for [(TPP)Fe^{III}–O–Fe^{III}(TPP)] with higher accuracy or in different space groups have been reported by Swepston & Ibers, 1985; Kooijmann *et al*., 2007 (CSD Private Communication, #667666); and Peters *et al*., 2019.
7. Swepston PN and Ibers JA. *Acta Crystallogr.* 1985; **C41**: 671–673.
8. Peters MK, Näther C and Herges R. *Acta Crystallogr.* 2019; **E75**: 930–933.
9. Kiong-Lam L, Buchler JW, Kenny JE and Scheidt WR. *Inorg. Chim. Acta* 1986; **123**: 91–97.
10. Cheng L, Lee J, Powell DR and Richter-Addo GB. *Acta Crystallogr.* 2004; **E60**: m1340–m1342.
11. Carroll JM and Norton JR. *J. Am. Chem. Soc.* 1992; **114**: 8744–8745.
12. Evans DR and Reed CA. *J. Am. Chem. Soc.* 2000; **122**: 4660–4667.
13. Goff H and Morgan LO. *Inorg. Chem.* 1976; **15**: 3180–3181.
14. Miller JR, Taies JA and Silver J. *Inorg. Chim. Acta* 1987; **138**: 205–214.
15. Kurtz DM. *Chem. Rev.* 1990; **90**: 585–606.
16. Scheidt WR, Cheng B, Safo MK, Cukiernik F, Marchon JC and Debrunner PG. *J. Am. Chem. Soc.* 1992; **114**: 4420–4421.
17. Evans DR, Mathur RS, Heerwegh K, Reed CA and Xie Z. *Angew. Chem., Int. Ed. Engl.* 1997; **36**: 1335–1337.
18. Ivanca MA, Lappin AG and Scheidt WR. *Inorg. Chem.* 1991; **30**: 711–718.
19. Fleischer EB, Palmer JM, Srivastava TS and Chatterjee A. *J. Am. Chem. Soc.* 1971; **93**: 3162–3167.
20. Melin F, Boudon C, Lo M, Schenk KJ, Bonin M, Ochsenbein P, Gross M and Weiss J. *J. Porphyrins Phthalocyanines* 2007; **11**: 212–221.
21. Johnson MR, Seok WK, Ma W, Slebodnick C, Wilcoxen KM and Ibers JA. *J. Org. Chem.* 1996; **61**: 3298–3303.
22. Kadish KM, Larson G, Lexa D and Momenteau M. *J. Am. Chem. Soc.* 1975; **97**: 282–288.
23. Forshey PA and Kuwana T. *Inorg. Chem.* 1981; **20**: 693–700.
24. Rodgers KR, Reed RA, Su YO and Spiro TG. *Inorg. Chem.* 1992; **31**: 2688–2700.

25. Kadish KM, Autret M, Ou Z, Tagliatesta P, Boschi T and Fares V. *Inorg. Chem.* 1997; **36**: 204–207.
26. Rywkin S, Hosten CM, Lombardi JR and Birke RL. *Langmuir* 2002; **18**: 5869–5880.
27. Bizzarri AR and Cannistraro S. In *Surface-Enhanced Raman Scattering: Physics and Applications*, Kneipp K, Moskovits M, Kneipp H. (Eds.) Springer: Berlin, Heidelberg, 2006; pp. 279–296.
28. Phillippi MA and Goff HM. *J. Am. Chem. Soc.* 1979; **101**: 7641–7643.
29. Chang D, Cocolios P, Wu YT and Kadish KM. *Inorg. Chem.* 1984; **23**: 1629–1633.
30. Gans P, Buisson G, Duee E, Marchon JC, Erler BS, Scholz WF and Reed CA. *J. Am. Chem. Soc.* 1986; **108**: 1223–1234.
31. Collman JP, Wagenknecht PS and Hutchison JE. *Angew. Chem. Int. Ed. Engl.* 1994; **33**: 1537–1554.
32. Rosenthal J and Nocera DG. In *Prog. Inorg, Chem.*, Karlin KD. (Ed.), 2007; pp. 483–544.
33. Sorokin AB. *Bioinorg. React. Mech.* 2012; **8**: 59–84.
34. Guchhait T, Sasmal S, Khan FST and Rath SP. *Coord. Chem. Rev.* 2017; **337**: 112–144.
35. Khan FS, Guchhait T, Sasmal S and Rath SP. *Dalton Trans.* 2017; **46**: 1012–1037.
36. Sorokin AB. *Coord. Chem. Rev.* 2019; **389**: 141–160.
37. Landrum JT, Grimmett D, Haller KJ, Scheidt WR and Reed CA. *J. Am. Chem. Soc.* 1981; **103**: 2640–2650.
38. Deng Y, Chang CJ and Nocera DG. *J. Am. Chem. Soc.* 2000; **122**: 410–411.
39. Pistorio BJ, Chang CJ and Nocera DG. *J. Am. Chem. Soc.* 2002; **124**: 7884–7885.
40. Hodgkiss JM, Chang CJ, Pistorio BJ and Nocera DG. *Inorg. Chem.* 2003; **42**: 8270–8277.
41. Chang CJ, Loh ZH, Shi C, Anson FC and Nocera DG. *J. Am. Chem. Soc.* 2004; **126**: 10013–10020.
42. Rosenthal J, Pistorio BJ, Chng LL and Nocera DG. *J. Org. Chem.* 2005; **70**: 1885–1888.
43. Ghosh SK, Patra R and Rath SP. *Inorg. Chem.* 2008; **47**: 10196–10198.
44. Ghosh SK, Patra R and Rath SP. *Inorg. Chem.* 2010; **49**: 3449–3460.
45. Ghosh SK, Patra R and Rath SP. *Inorg. Chim. Acta* 2010; **363**: 2791–2799.
46. Sil D, Khan FS and Rath SP. *Chem.— Eur. J.* 2016; **22**: 14585–14597.
47. Steiner T. *Angew. Chem., Int. Ed.* 2002; **41**: 48–76.
48. Khan FS, Pandey AK and Rath SP. *Chem. — Eur. J.* 2016; **22**: 16124–16137.
49. Wollmann RG and Hendrickson DN. *Inorg. Chem.* 1978; **17**: 926–930.
50. Ivashin NV, Shulga AM, Terekhov SN and Dzilinski K. *Spectrochim. Acta A* 1996; **52**: 1603–1614.
51. Richman RM and Peterson MW. *J. Am. Chem. Soc.* 1982; **104**: 5795–5796.
52. Peterson MW and Richman RM. *Inorg. Chem.* 1985; **24**: 722–725.
53. Brémard C, Kowalewski P, Merlin JC and Moreau S. *J. Raman Spectrosc.* 1992; **23**: 325–333.
54. Chin D-H, La Mar GN and Balch AL. *J. Am. Chem. Soc.* 1980; **102**: 5945–5947.
55. Peterson MW, Rivers DS and Richman RM. *J. Am. Chem. Soc.* 1985; **107**: 2907–2915.
56. Bergamini P, Sostero S, Traverso O, Deplano P and Wilson LJ. *J. Chem. Soc., Dalton Trans.* 1986: 2311–2314.
57. Guest CR, Straub KD, Hutchinson JA and Rentzepis PM. *J. Am. Chem. Soc.* 1988; **110**: 5276–5280.
58. Shantha PK and Verma AL. *Inorg. Chem.* 1996; **35**: 2723–2725.
59. Rosenthal J, Luckett TD, Hodgkiss JM and Nocera DG. *J. Am. Chem. Soc.* 2006; **128**: 6546–6547.
60. Guo C-C. *Acta Chim. Sin.* 1994; **52**: 367–371.
61. Guo C-C. *J. Catal.* 1998; **178**: 182–187.
62. Guo C-C, Liu X-Q, Li Z-P and Guo D-C. *Appl. Catal., A* 2002; **230**: 53–60.
63. Guo C-C, Peng Q, Liu Q and Jiang G. *J. Mol. Catal. A* 2003; **192**: 295–302.
64. Hu H-Y, Jiang Q, Liu Q, Song J-X, Lin W-Y and Guo C-C. *J. Porphyrins Phthalocyanines* 2006; **10**: 948–952.
65. Tabor E, Połtowicz J, Pamin K, Basąg S and Kubiak W. *Polyhedron* 2016; **119**: 342–349.
66. Luo W, Liu D, Sun J, Deng W, Sheng W, Liu Q and Guo C-C. *Chin. J. Chem. Eng.* 2014; **22**: 509–515.
67. Luo W, Sun J, Ye J, Deng W, Liu Q and Guo C-C. *J. Ind. Eng. Chem.* 2014; **20**: 3061–3067.
68. Cordes C, Morganti M, Klawitter I, Schremmer C, Dechert S and Meyer F. *Angew. Chem., Int. Ed.* 2019; **58**: 10855–10858.
69. Gallagher KJ, Espinal-Viguri M, Mahon MF and Webster RL. *Adv. Synth. Catal.* 2016; **358**: 2460–2468.
70. Aguiar A, Ribeiro S, Silva AMN, Cunha-Silva L, de Castro B, Silva AMG and Balula SS. *Appl. Catal. A* 2014; **478**: 267–274.
71. Fidalgo-Marijuan A, Barandika G, Bazán B, Urtiaga MK, Larrea ES, Iglesias M, Lezama L and Arriortua MI. *Dalton Trans.* 2015; **44**: 213–222.
72. Settin MF and Fanning JC. *Inorg. Chem.* 1988; **27**: 1431–1435.
73. Ellison MK, Schulz CE and Scheidt WR. *Inorg. Chem.* 1999; **38**: 100–108.
74. Xu N, Campbell ALO, Powell DR, Khandogin J and Richter-Addo GB. *J. Am. Chem. Soc.* 2009; **131**: 2460–2461.
75. Hou Y, Zhu Y, Sun J, Zhang X, Tian Y and Jiang J. *CrystEngComm* 2015; **17**: 4699–4704.

76. Lee HM, Olmstead MM, Gross GG and Balch AL. *Cryst. Growth Des.* 2003; **3**: 691–697.
77. Litvinov AL, Konarev DV, Kovalevsky AY, Lapshin AN, Yudanova EI, Drichko NV, Coppens P and Lyubovskaya RN. *Eur. J. Inorg. Chem.* 2003: 3914–3917.
78. Konarev DV, Khasanov SS and Lyubovskaya RN. *J. Porphyrins Phthalocyanines* 2010; **14**: 293–297.
79. Williams LJ, Dowgiallo A-M and Knappenberger KL. *Phys. Chem. Chem. Phys.* 2013; **15**: 11840–11845.
80. Wang Y, Ang PL, Wong C-Y and Yip JHK. *Chem. — Eur. J.* 2018; **24**: 18623–18628.
81. Abdullin D, Fleck N, Klein C, Brehm P, Spicher S, Lützen A, Grimme S and Schiemann O. *Chem. — Eur. J.* 2019; **25**: 2586–2596.
82. Suzuki M, Tsuge K, Sasaki Y and Imamura T. *Chem. Lett.* 2003; **32**: 564–565.
83. Takeuchi M, Imada T and Shinkai S. *J. Am. Chem. Soc.* 1996; **118**: 10658–10659.
84. Takeuchi M, Imada T and Shinkai S. *Bull. Chem. Soc. Jpn.* 1998; **71**: 1117–1123.
85. Gao D, Li J-Z, Yu R-Q and Zheng G-D. *Anal. Chem.* 1994; **66**: 2245–2249.
86. Schappacher M and Deffieux A. *J. Am. Chem. Soc.* 2011; **133**: 1630–1633.
87. Schappacher M and Deffieux A. *Macromolecules* 2011; **44**: 4503–4510.
88. Schappacher M, Deffieux A and Le Meins J-F. *Polym. Chem.* 2013; **4**: 458–461.
89. Tian X, Lin C, Zhong Z, Li X, Xu X, Liu J, Kang L, Chai G and Yao J. *Cryst. Growth Des.* 2019; **19**: 3279–3287.
90. Wang DH, Pan JN, Li HH, Liu JJ, Wang YB, Kang LT and Yao JN. *J. Mater. Chem. A* 2016; **4**: 290–296.
91. Smalley JW, Birss AJ, Szmigielski B and Potempa J. *Microbiology* 2006; **152**: 1839–1845.
92. Smalley JW, Birss AJ, Szmigielski B and Potempa J. *Arch. Biochem. Biophys.* 2007; **465**: 44–49.
93. Gorka AP, de Dios A and Roepe PD. *J. Med. Chem.* 2013; **56**: 5231–5246.
94. Leed A, DuBay K, Ursos LMB, Sears D, de Dios AC and Roepe PD. *Biochemistry* 2002; **41**: 10245–10255.
95. de Dios AC, Casabianca LB, Kosar A and Roepe PD. *Inorg. Chem.* 2004; **43**: 8078–8084.
96. Kuter D, Benjamin SJ and Egan TJ. *J. Inorg. Biochem.* 2014; **133**: 40–49.
97. Bartczak TJ, Latos-Grażyński L and WysŁouch A. *Inorg. Chim. Acta* 1990; **171**: 205–212.
98. Hino T, Matsumoto Y, Nagano S, Sugimoto H, Fukumori Y, Murata T, Iwata S and Shiro Y. *Science* 2010; **330**: 1666.
99. Wasser IM, de Vries S, Moënne-Loccoz P, Schröder I and Karlin KD. *Chem. Rev.* 2002; **102**: 1201–1234.
100. Girsch P and de Vries S. *Biochim. Biophys. Acta* 1997; **1318**: 202–216.
101. Moënne-Loccoz P and de Vries S. *J. Am. Chem. Soc.* 1998; **120**: 5147–5152.
102. Moënne-Loccoz P, Richter O-MH, Huang H-W, Wasser IM, Ghiladi RA, Karlin KD and de Vries S. *J. Am. Chem. Soc.* 2000; **122**: 9344–9345.
103. Martens CF, Murthy NN, Obias HV and Karlin KD. *Chem. Commun.* 1996: 629–630.
104. Wasser IM, Martens CF, Verani CN, Rentschler E, Huang HW, Moenne-Loccoz P, Zakharov LN, Rheingold AL and Karlin KD. *Inorg. Chem.* 2004; **43**: 651–662.
105. Wei N, Lee D-H, Murthy NN, Tyeklar Z, Karlin KD, Kaderli S, Jung B and Zuberbuehler AD. *Inorg. Chem.* 1994; **33**: 4625–4626.
106. Wasser IM, Fry HC, Hoertz PG, Meyer GJ and Karlin KD. *Inorg. Chem.* 2004; **43**: 8272–8281.
107. Mihara N, Yamada Y, Takaya H, Kitagawa Y, Aoyama S, Igawa K, Tomooka K and Tanaka K. *Chem. —Eur. J.* 2017; **23**: 7508–7514.
108. Nanthakumar A, Fox S, Murthy NN, Karlin KD, Ravi N, Huynh BH, Orosz RD, Day EP, Hagen KS and Blackburn NJ. *J. Am. Chem. Soc.* 1993; **115**: 8513–8514.
109. Lee SC and Holm RH. *J. Am. Chem. Soc.* 1993; **115**: 11789–11798.
110. Ju TD, Ghiladi RA, Lee D-H, van Strijdonck GPF, Woods AS, Cotter RJ, Young VG and Karlin KD. *Inorg. Chem.* 1999; **38**: 2244–2245.
111. Ghiladi RA, Hatwell KR, Karlin KD, Huang H-W, Moënne-Loccoz P, Krebs C, Huynh BH, Marzilli LA, Cotter RJ, Kaderli S and Zuberbühler AD. *J. Am. Chem. Soc.* 2001; **123**: 6183–6184.
112. Kim E, Chufán EE, Kamaraj K and Karlin KD. *Chem. Rev.* 2004; **104**: 1077–1134.
113. Hematian S, Garcia-Bosch I and Karlin KD. *Acc. Chem. Res.* 2015; **48**: 2462–2474.
114. Nanthakumar A, Nasir MS, Karlin KD, Ravi N and Huynh Boi H. *J. Am. Chem. Soc.* 1992; **114**: 6564–6566.
115. Chishiro T, Shimazaki Y, Tani F and Naruta Y. *Chem. Commun.* (*Camb*) 2005: 1079–1081.
116. Fox S, Nanthakumar A, Wikström M, Karlin KD and Blackburn NJ. *J. Am. Chem. Soc.* 1996; **118**: 24–34.
117. Nanthakumar A, Fox S, Murthy NN and Karlin KD. *J. Am. Chem. Soc.* 1997; **119**: 3898–3906.
118. Scott MJ, Zhang HH, Lee SC, Hedman B, Hodgson KO and Holm RH. *J. Am. Chem. Soc.* 1995; **117**: 568–569.
119. Karlin KD, Nanthakumar A, Fox S, Murthy NN, Ravi N, Huynh BH, Orosz RD and Day EP. *J. Am. Chem. Soc.* 1994; **116**: 4753–4763.
120. Kim E, Helton ME, Wasser IM, Karlin KD, Lu S, Huang H-W, Moënne-Loccoz P, Incarvito CD, Rheingold AL, Honecker M, Kaderli S and

Zuberbühler AD. *Proc. Natl. Acad. Sci. USA*. 2003; **100**: 3623.
121. Kramarz KWN and Jack R. In *Prog. Inorg. Chem.*, Vol. 42, Karlin KD. (Ed.) John Wiley & Sons, Inc., 1994; pp. 1–65.
122. Kopf M-A, Neuhold Y-M, Zuberbuhler AD and Karlin KD. *Inorg. Chem.* 1999; **38**: 3093–3102.
123. Obias HV, van Strijdonck GPF, Lee D-H, Ralle M, Blackburn NJ and Karlin KD. *J. Am. Chem. Soc.* 1998; **120**: 9696–9697.
124. Halime Z, Kieber-Emmons MT, Qayyum MF, Mondal B, Gandhi T, Puiu SC, Chufán EE, Sarjeant AAN, Hodgson KO, Hedman B, Solomon EI and Karlin KD. *Inorg. Chem.* 2010; **49**: 3629–3645.
125. Hematian S, Kenkel I, Shubina TE, Durr M, Liu JJ, Siegler MA, Ivanovic-Burmazovic I and Karlin KD. *J. Am. Chem. Soc.* 2015; **137**: 6602–6615.
126. Maia LB and Moura JJG. *Chem. Rev.* 2014; **114**: 5273–5357.
127. Castello PR, David PS, McClure T, Crook Z and Poyton RO. *Cell Metab*. 2006; **3**: 277–287.
128. Hematian S, Siegler MA and Karlin KD. *J. Am. Chem. Soc.* 2012; **134**: 18912–18915.
129. Hematian S, Siegler MA and Karlin KD. *J. Biol. Inorg. Chem.* 2014; **19**: 515–528.
130. Liston DJ, Kennedy BJ, Murray KS and West BO. *Inorg. Chem.* 1985; **24**: 1561–1567.
131. Oyaizu K, Haryono A, Nishimura Y, Yamamoto K and Tsuchida E. *Bull. Chem. Soc. Jpn.* 1999; **72**: 1781–1784.
132. Chufán EE, Verani CN, Puiu SC, Rentschler E, Schatzschneider U, Incarvito C, Rheingold AL and Karlin KD. *Inorg. Chem.* 2007; **46**: 3017–3026.
133. Hamer M, Tomba JP and Rezzano IN. *Sens. Actuators B*2014; **193**: 121–127.
134. Li M, Shang M, Duval HF and Scheidt WR. *Acta Crystallogr.* 2000; **C56**: 1206–1207.
135. Li A-R, Wei H-H and Gang L-L. *Inorg. Chim. Acta* 1999; **290**: 51–56.
136. Jiao X-D, Huang J-W, Ji L-N, Luo B-S and Chen L-R. *J. Inorg. Biochem.* 1997; **65**: 229–233.
137. Gold A, Jayaraj K, Doppelt P, Fischer J and Weiss R. *Inorg. Chim. Acta* 1988; **150**: 177–181.
138. Amanullah S, Saha P, Saha R and Dey A. *Inorg. Chem.* 2019; **58**: 152–164.
139. Cheng B, Hobbs JD, Debrunner PG, Erlebacher J, Shelnutt JA and Scheidt WR. *Inorg. Chem.* 1995; **34**: 102–110.
140. Patra R, Bhowmik S, Ghosh SK and Rath SP. *Eur. J. Inorg. Chem.* 2009: 654–665.
141. Schaefer WP, Ellis PE, Lyons JE and Shaikh SN. *Acta Crystallogr.* 1995; **C51**: 2252–2255.
142. Sainna MA, Sil D, Sahoo D, Martin B, Rath SP, Comba P and de Visser SP. *Inorg. Chem.* 2015; **54**: 1919–1930.
143. Ghosh SK and Rath SP. *J. Am. Chem. Soc.* 2010; **132**: 17983–17985.
144. Bhowmik S, Ghosh SK, Layek S, Verma HC and Rath SP. *Chem. — Eur. J.* 2012; **18**: 13025–13037.
145. Ghosh SK, Bhowmik S, Sil D and Rath SP. *Chem. — Eur. J.* 2013; **19**: 17846–17859.
146. Ju TD, Woods AS, Cotter RJ, Moënne-Loccoz P and Karlin KD. *Inorg. Chim. Acta* 2000; **297**: 362–372.
147. Wysłouch A, Latos-Grażyński L, Grzeszczuk M, Drabent K and Bartczak T. *J. Chem. Soc., Chem. Commun.* 1988: 1377–1378.